Remote Sensing of Environment 224 (2019) 333–351

Contents lists available at ScienceDirect

Remote Sensing of Environment

journal homepage: www.elsevier.com/locate/rse

A highly automated algorithm for wetland detection using multi-temporal optical satellite data

Christina Ludwig, Andreas Walli, Christian Schleicher, Jürgen Weichselbaum, Michael Riffler*

GeoVille Information Systems and Data Processing GmbH, Sparkassenplatz 2, 6020 Innsbruck, Austria

ARTICLE INFO

Keywords:
Wetland detection
Water body mapping
Split-based image thresholding
Image compositing
Sentinel-2
Water frequency
Wetness frequency
WWPI

ABSTRACT

Wetlands are valuable ecosystems providing a variety of important ecosystem services such as food supply and flood control. Due to increasing anthropogenic influences and the impact of climate change, wetlands are increasingly threatened and degraded. An effective monitoring of wetlands is therefore necessary to preserve and restore these endangered ecosystems. Earth Observation (EO) data offer a great potential to support cost-effective and large-scale monitoring of wetlands. Current state-of-the-art methods for wetland mapping, however, require large training data and manual effort and can therefore only be locally applied. The focus of this study is to evaluate a methodology for large-scale and highly automated wetland mapping based on current EO data streams. For this purpose, an algorithm for water and wetness detection based on multi-temporal optical imagery and topographic data is presented. Suitable spectral indices sensitive to water and wetness were identified using feature selection methods based on mutual information between optical indices and occurrence of water and wetness. In combination with the Topographic Wetness Index (TWI), these were used to derive monthly water and wetness masks using a dynamic thresholding approach. Aggregating all observations corrected for seasonal bias yielded flooding and wetness frequencies and the Water Wetness Presence (or Probability) Index (WWPI) as an indicator for wetland occurrence or a pre-inventory. To demonstrate the applicability of the proposed method, the algorithm is demonstrated at three study sites with different wetland types in Kenya/Uganda, Algeria, and Austria using Sentinel-2 MultiSpectral Instrument (MSI) imagery. For all sites, the overall accuracy was above 92%. User's and producer's accuracies were higher for water (> 96%) than for wetness (> 75%). Due to the high degree of automation and low processing time, the proposed method is applicable on a large scale and has already been applied during the production of the Copernicus High Resolution Water-Wetness Layer and within the European Space Agency (ESA) project GlobWetland Africa.

1. Introduction

Wetlands are very important ecosystems providing habitat for a variety of flora and fauna as well as many valuable ecosystem services such as flood control, water purification, and food supply. However, with increasing human water demand for agriculture, livestock, and settlements, wetlands are becoming increasingly threatened and degraded especially in water scarce regions (Ramsar Convention, 2016). Effects of climate change such as temperature increases and changes in precipitation patterns, are expected to have a significant impact on the occurrence, structure and functions of wetlands (Erwin, 2009), especially in their role as an organic carbon sink (Junk et al., 2013).

Thus, for preservation and restoration of wetlands, a cost-effective and efficient monitoring of these ecosystems is necessary. Satellite data offers great potential for wetland monitoring and has been the subject of many studies (Tiner et al., 2015). Yet, a large-scale monitoring system that captures the seasonal dynamics and long-term trends of wetlands has not yet been implemented. Pekel et al. (2016) produced a global surface water map based on the Landsat archive. Although being a first step towards large-scale monitoring of water-related ecosystems, it is not sufficient for wetland monitoring, since only the spatio-temporal distribution of open surface water is covered and the mapping of wet soils is missing.

Due to their high spatial heterogeneity and temporal dynamics, wetlands are very difficult to map using remote sensing imagery (Ozesmi and Bauer, 2002). Seasonal or daily water level changes make the extent and spectral signature of wetlands highly dynamic. Therefore, mono-temporal classification approaches are not sufficient to fully

* Corresponding author.
E-mail addresses: ludwig@geoville.com (C. Ludwig), walli@geoville.com (A. Walli), schleicher@geoville.com (C. Schleicher), weichselbaum@geoville.com (J. Weichselbaum), riffler@geoville.com (M. Riffler).

https://doi.org/10.1016/j.rse.2019.01.017
Received 17 October 2017; Received in revised form 30 November 2018; Accepted 13 January 2019
Available online 22 February 2019
0034-4257/

capture the temporal dynamics of wetlands and to delineate their extents. Multi-temporal imagery increases the accuracy of classification results (Ozesmi and Bauer, 2002) and enables the monitoring of the seasonal dynamics of the water regime of the wetland. Imagery from the Landsat 8 Operational Land Imager (OLI) and Sentinel-2 Multi-Spectral Instrument (MSI) provide the necessary spatial and temporal resolution to facilitate the implementation of an effective wetland monitoring methodology.

Water and wet surfaces characteristically show strong absorption in the near infrared (NIR) and shortwave infrared (SWIR) spectrum, while dry soils and vegetation are highly reflecting radiation in these spectral ranges (Tiner et al., 2015). Hence, these spectral bands and indices derived thereof have a high potential for measuring moisture levels in soils and vegetation and are popular indicators for water body delineation and wetland mapping (Kulawardhana et al., 2007; Islam et al., 2008; Bwangoy et al., 2010; Davranche et al., 2013). Using these bands for classification is also advantageous, since radiation in this spectral range is usually less affected by atmospheric aerosol scattering than the visible spectral region (Gao, 1996).

Based on these physical principles, the Normalized Difference Water Index (NDWI) including the green and near-infrared radiation was developed for water body mapping by McFeeters (1996). Xu (2006) modified this index by substituting the NIR band with the shortwave infrared 1 (SWIR1) band calling it the modified Normalized Difference Water Index (mNDWI). This modification considerably improves the detectability of open water bodies and reduces confusion with built-up areas. NDWI and mNDWI have successfully been applied for water body mapping in several studies (Li et al., 2013; Chen et al., 2013; Rokni et al., 2014; Jiang et al., 2014; Tetteh and Schönert, 2015; Donchyts et al., 2016). Furthermore, the Tasselled Cap Wetness Index (TCWI) and Tasselled Cap Brightness Index (TCBI) have been proven to be suitable for the detection of inundated areas (Orodyne and Friedl, 2008; Tana et al., 2013; Islam et al., 2008). The Automated Water Extraction Index (AWEI) was developed for Landsat 5 Thematic Mapper (TM) bands to maximize the separability of water and non-water land cover classes using a steady threshold of zero and is especially targeted at improving the separability of water and shadows (Feyisa, 2014).

For wetland mapping, additional spectral indices that are particularly sensitive to moisture level changes in soils and vegetation have been applied. Gao (1996) developed the NDWI, also known as the Land Surface Water Index (LSWI) or Normalized Difference Moisture Index (NDMI), which quantifies moisture levels in vegetation and exhibits a positive correlation with surface water and soil moisture (Zhao et al., 2009). Furthermore, Davranche et al. (2013) proposed the Modified Water Index (MWI), Modified Water Impoundment Index (MWII), and Modified Index of Free Water (MIFW) for detecting wet soils. The Shortwave Angle Slope Index (SASI) (Khannaa et al., 2007) and the Normalized Multi-band Drought Index (NMDI) (Wang and Qu, 2007) have also been used to distinguish changes in plant water content and soil moisture.

Image enhancement techniques such as RGB False Color Composites (FCCs) of spectral bands or band ratios are other approaches which have been used for water and wetland mapping. Kulawardhana et al. (2007) and Islam et al. (2008) used FCCs based on the red, NIR and SWIR1 bands to highlight wetlands for manual digitization. By applying a Hue-Saturation-Value (HSV) transformation, FCCs can also be used for automated wetland classification. This has been done for water detection by Pekel (2014) using the SWIR1, NIR, and red bands and by Jiang et al. (2011) using the Normalized Difference Vegetation Index (NDVI), Normalized Difference Build-up Index (NDBI), and mNDWI.

Even though a variety of spectral indices for the detection of water and wet soils (hereafter referred to as *wetness*) is available, wetlands are still easily confused with other upland land cover types such as forests and shadows, since they share similar spectral profiles (Ozesmi and Bauer, 2002; Tiner et al., 2015). Including additional ancillary data into the classification considerably reduces these errors and improves classification results (Ozesmi and Bauer, 2002). Since the occurrence of wetlands strongly depends on the topography of the landscape, topographic indices have been widely used for water and wetland mapping (Corcoran et al., 2011; Bwangoy et al., 2010; Fluet-Chouinard et al., 2015). Topographic information has also been used to reduce commission errors within non-flood prone areas using slope (Li and Chen, 2005), the Height Above Nearest Drainage (HAND) index (Martinis et al., 2009) and other features derived from a Digital Elevation Model (DEM) such as sinks and streamlines (Landmann et al., 2010).

The most common classification methods for wetland mapping are unsupervised (Dogan et al., 2009; Chen et al., 2014), supervised (Bwangoy et al., 2010; Corcoran et al., 2011; Fluet-Chouinard et al., 2015) and hybrid classification combining supervised and unsupervised classification approaches (Mwita et al., 2012; Lane et al., 2014). Chen et al. (2014) used unsupervised ISODATA classification based on a moderate resolution imaging spectroradiometer (MODIS) NDVI time series to classify different wetland types. Random Forest (Breiman, 2001) is the most popular supervised classification method for wetland mapping and has been applied by Bwangoy et al. (2010) to map wetlands in the Congo Basin. Li and Chen (2005) showed that an integrated classification approach using rule-based classification, decision tree classifiers, and separate classification of optical and Synthetic Aperture Radar (SAR) (C-band) data leads to good mapping results for bogs and fens.

Kulawardhana et al. (2007) used a rule-based classification approach based on static thresholds of spectral indices to map wetlands, but they did not yield satisfying classification results. Classification methods based on dynamic thresholding were more successful. Otsu thresholding is one of the most popular classification methods for water mapping using SAR imagery, since it is computationally relatively inexpensive, fast, and reliable (Martinis et al., 2009). Donchyts et al. (2016) used Otsu thresholding and a Random Forest classifier based on the mNDWI and HAND index to successfully map water bodies. Tile-based image thresholding has been developed by Martinis et al. (2009) for water body mapping using SAR imagery, but has not been tested for water and wetness detection using optical imagery yet.

A major challenge when mapping wetlands is the diversity of existing definitions. Tiner (2016) provides an exhaustive review of various wetland definitions. According to the author, no unique or scientific definition for wetlands does exist but rather depends on the field of study, reporting obligations, etc. According to Charman (2002), wetlands can be defined by three different aspects: hydrology, soil type, and vegetation. In this study, we focus on the hydrological definition of wetlands by separating wetlands from other land cover types in separating dry and wet soils as well as open surface water based on spectral indices which physically link measured reflectance to moisture levels in soil and vegetation. However, in contrast to most other wetland classification methods, the approach presented herein does not rely on absolute reference values to distinguish wetness from dryness (e.g., static thresholds of soil moisture or plant water content or supervised learning algorithms), but delineates wetlands based on their spatial context, i.e., the contrast between wet and dry surfaces. This means that wetlands are mapped in relative instead of absolute terms, which is crucial for making the proposed method applicable for wetland mapping in different bio-geographic regions without the need for extensive training data. Furthermore, wetlands are fuzzy objects with no clear boundary, thus, the one right threshold to delineate them does not exist, but a range of plausible thresholds needs to be considered (Bennett, 2001).

Current state-of-the-art methods for wetland mapping require large training data and manual effort which is why they can only be applied locally. The aim of this study is to investigate whether wetland mapping can be performed for large areas and within different bio-geographic regions in a highly automated way and without the need for extensive training data. For this purpose, an algorithm for water and wetness detection using multi-temporal optical imagery and topographic data to

support large-scale mapping exercises in a cost-effective manner is proposed. It is demonstrated using Sentinel-2 MSI imagery, but is also applicable to other imagery with similar spatial and temporal resolution (and spectral channels) such as the Landsat missions. The spectral signatures of water and wet surfaces are enhanced by applying different image enhancement methods to a combination of spectral and topographic indices derived from monthly image composites. A modified form of tile-based image thresholding is subsequently used to delineate open water and wet surfaces. To ensure the identification of a valid threshold, locally adaptable constraints to the classifier are introduced to guide the detection algorithm. Applied to the whole time series, this yields monthly water and wet soil masks. These are subsequently used to compute the overall water and wetness frequency maps, as well as the Water and Wetness Presence (or Probability) Index (WWPI) which serves as a pre-inventory of wetlands. To evaluate the performance of the method in different bio-geographical regions, results are presented for three different study sites in Africa and Europe. The first site is located in a dry climate with sparse vegetation, the second one in a tropical climate with dense vegetation and the third one in a temperate central European climate. The proposed method is a first step towards the implementation of a monitoring system to track long-term trends in wetlands and the creation of a global wetland inventory.

The outline of the paper is as follows: In Section 2, the three study sites and the available input data is described. Subsequently, the methods for image compositing, the calculation of water and wetness probabilities, tile-based image thresholding and validation are explained. The classification results are presented and discussed in Sections 3 and 4.

2. Data and methods

2.1. Study sites

To demonstrate the suitability and general applicability of the method for the detection of wetland areas in different bio-geographic areas, the proposed approach has been tested and validated at three different locations in Africa and Europe. The first site is located in a dry climate with sparse vegetation, the second one in a tropical climate with dense vegetation and the third one in a temperate central European climate. The focus on these continents is caused by the fact that the methodology has been developed within the ESA project “GlobWetland Africa” for which dozens of wetland areas throughout Northern, Western, Eastern and Central Africa are mapped as well as for the production of the European Environmental Agency (EEA) Pan-European High Resolution Layers (HRL) “Water and Wetness”.

2.1.1. El Kala Wetland System, Algeria

The El-Kala Wetland System is a complex of wetlands, lakes and rivers, marshes and sea inlets situated within the El-Kala National Park (Smart and Hollis, 1990) (Fig. 1A). The climate is temperate with hot, dry summers and rain fall mainly occurring in winter (Kottek et al., 2006). The two freshwater lakes in the East, Lac Tonga and Lac Oubeïra, are part of “The Ramsar List of Wetlands of International Importance” (Smart and Hollis, 1990). A considerable part of Lake Tonga is drying out during summer as a consequence of water extraction leaving only reed beds behind. The Marais de la Mekhada is a freshwater marsh located within the Mafragh floodplain which is connected to the Mediterranean Sea through a narrow channel. 80% of the marsh is vegetated by rushes and during the wet season it reaches a water depth of up to 1 m. The Oum Lâagareb wetland is a densely forested floodplain peat land which is rarely found in the area. Most wetlands within the complex are important nesting and wintering grounds for birds and support a range of rare plant and animal species. The wetlands are threatened by human intervention in the form of infrastructure development and excessive water extraction for irrigation (Ramsar Convention, 2001).

2.1.2. Sio-Siteko Wetland, Uganda/Kenya

The Sio-Siteko Wetland is located at the northern shore of Lake Victoria spanning the boarder of Uganda and Kenya (Fig. 1B). The predominant climate is equatorial and monsoonal according to Köppen-Geiger (Kottek et al., 2006). Rainfall occurs throughout the year with two rainy seasons around April and October. The wetland covers an area of 8.900 ha and consists of several interconnected wetland subsystems. The Sio river flows through the wetland and drains into Lake Victoria. The wetlands provide many important ecosystem services such as the supply of fresh water and food, water purification, and provision of habitats for plants and animals. Due to human interventions like canalization, extraction of water for agriculture, livestock, and cities, the wetlands are threaded by sinking water quality and fluctuations in the water level, which are likely to have a negative impact on flora, fauna, and the ecosystem services the wetland provides (MEMR, 2012).

2.1.3. Lake Neusiedl, Austria

Lake Neusiedl is located within the National Park Neusiedler See–Seewinkel spanning the Austrian-Hungarian border (Fig. 1C). The climate is temperate with cool, rainy summers (Kottek et al., 2006). The lake is 36 km long and 6–12 km wide covering an area of 315 km^2. The lake is very shallow reaching a maximum water depth of 1.8 m. It is the largest endorheic lake in Central Europe and one of the two steppe lakes in Europe (Beiwl and Mühlmann, 2008). In addition to precipitation and groundwater inflow, the lake is fed by the Wolka in the North. Its only outflow is the Hansag channel in the South. The lake is almost completely surrounded by reed beds and marshes, which provide a unique habitat for plants and animals especially birds. There is a complex of 80 small lakes and remnant salt meadows in the surroundings of the lake, some of which are only seasonally flooded. Reed harvesting, bird hunting, fishing, and tourism are the main form of human intervention. In addition, the area around the lake is extensively farmed (Ramsar Convention, 2001).

2.2. Data

2.2.1. Sentinel-2 MSI

The Sentinel-2 MSI measures the Earth's reflected radiance in 13 spectral bands covering the visible, near-infrared, and short wave infrared spectrum. Sentinel-2 is a twin-orbit constellation (Sentinel-2A/B) with a revisit time of approximately five days at the equator and even shorter periods towards the poles. Sentinel-2 data is available as a Level-1C product with radiometric and geometric corrections applied including conversion to Top-Of-Atmosphere (TOA) reflectance, orthorectification and spatial registration (European Space Agency, 2015). For the three study sites, all available Sentinel-2 observations from December 2015 until July 2017 with a cloud coverage of less than 80% were considered.

For the Sio-Siteko Wetland, 64 Sentinel-2 observations between December 2015 and June 2017 are available. These data were sufficient to derive almost complete monthly image composites for all months but April of both years. There are 69 Sentinel observations covering the El-Kala Wetland Complex between December 2015 and June 2017. Due to more frequent cloud coverage in winter, the number of observations during this season is reduced with only two scenes with less than 80% cloud cover in December 2016 and none in January 2017. For Lake Neusiedl, 130 Sentinel-2 observations from two granules were processed. Due to clouds and snow, the number of observations is also reduced during winter. This bias is, however, accounted for in the calculation of the overall water and wetness frequencies by normalizing the frequencies on a seasonal basis (see Section 2.3.6).

2.2.2. Digital elevation model

A DEM generated from the NASA Shuttle Radar Topography Mission (SRTM) in 2000 was used to calculate the Topographic Wetness Index (TWI) (see Section 2.3.3). The SRTM DEM was derived using radar

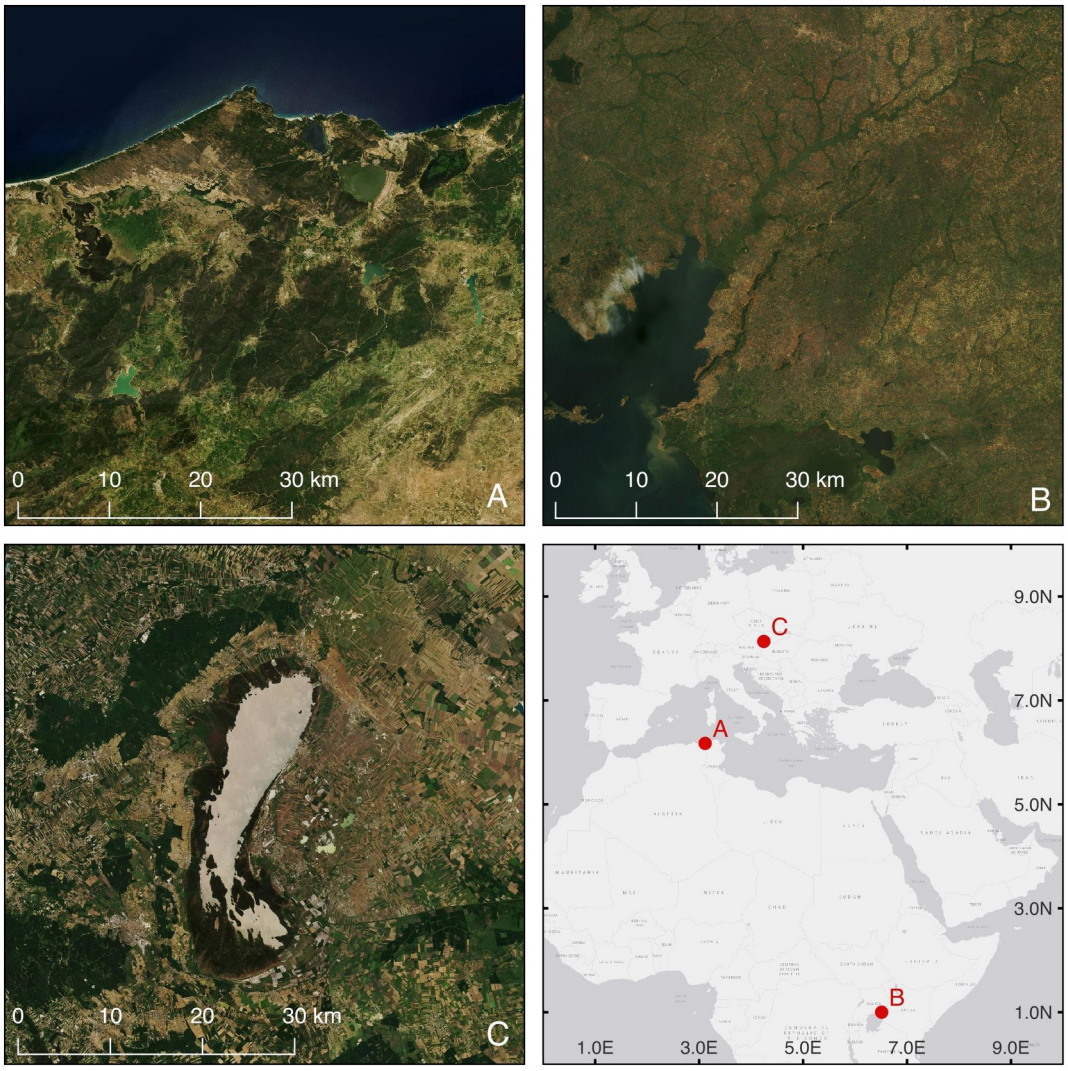

Fig. 1. True-color images of the study sites: A) El-Kala Wetland Complex, Algeria. B) Sio-Siteko Wetland, Uganda/Kenya. C) Lake Neusiedl, Austria. The designations of the sites reflect the order of presentation.
Source: Imagery: MapQuest OpenAerial.

interferometry and was processed at 1-arc-second resolution. The absolute vertical accuracy of the SRTM DEM is less than 9 m with the greatest errors occurring in steep terrain and smooth sandy surfaces (Farr et al., 2007).

2.2.3. Training data

The selection of suitable indices for water and wetness detection required training data sets with land cover information. For each study site, sample points for water, wet surfaces with varying degrees of vegetation cover and other land cover classes such as forest and urban areas were created. The sample points were manually placed and labelled using available in-situ maps, Google Earth Imagery and the Global Lakes and Wetlands Database (GLWD) provided by the World Wildlife Fund (WWF). The GLWD compromises large lakes, man-made reservoirs, smaller water bodies, and their maximum extents as well as different types of wetlands worldwide with a spatial resolution of 30 arc-seconds (World Wildlife Fund, 2016). In addition, spectral indices derived from selected monthly Sentinel-2 composites (see Section 2.3.1.3) were also used as a reference to better distinguish dry from wet surfaces.

2.3. Methods

The proposed algorithm is based on a multi-temporal classification approach (Fig. 2). Pre-processing includes cloud masking and monthly image compositing (see Section 2.3.1.3), calculation of monthly water and wetness (wet soil) probabilities and derivation of monthly water and wetness extents using tile-based image thresholding (see Section 2.3.5). Aggregating these extents yields the water and wetness frequencies for the whole investigation period from which the Water Wetness Presence (or Probability) Index (WWPI) is derived (see Section 2.3.6). Details of the processing steps are explained in the following section.

One of the assumptions behind the proposed method is a sufficient contrast between water, wet soils (wetness) and their dry surroundings. For water, this is usually given due to the distinctive spectral signature compared to other land cover types. In the case of wetness, this contrast is usually not as pronounced, but can be increased using image enhancement techniques and additional topographic information. Furthermore, the selection of satellite observations for the analyses need to cover the full hydrological year to derive a representative classification result.

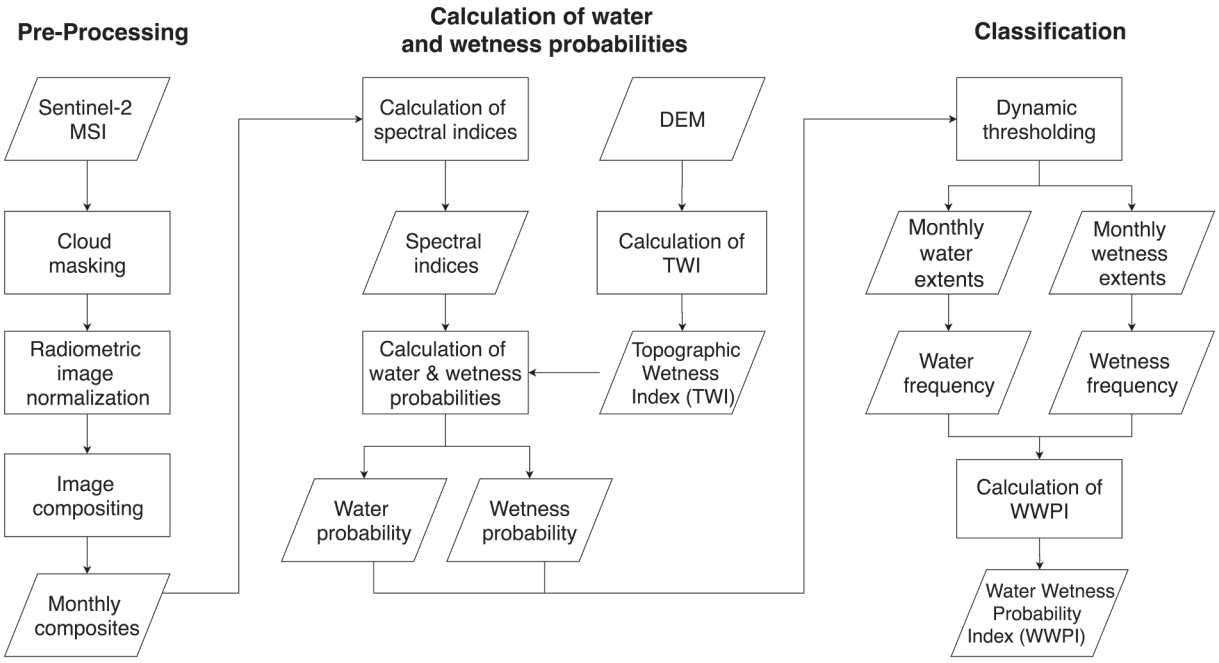

Fig. 2. Graphical workflow diagram of the algorithm for water and wetness detection.

Table 1
RMSE between two Landsat 7 scenes taken on September 16th and October 18th 2012 before (original images) and after histogram matching using different reference images.

Band	Original images	25th precentile	Best scene	Best scene within season
BLUE	102.54	72.67	95.47	100.24
GREEN	167.24	87.44	101.78	124.02
RED	278.35	132.55	148.13	193.00
NIR	536.75	372.61	425.25	360.93
SWIR1	372.82	202.89	198.34	255.73
SWIR2	251.77	162.93	177.28	208.42

2.3.1. Pre-processing

2.3.1.1. Cloud and cloud shadow detection. In order to derive monthly image composites with a minimum amount of atmospheric contamination, clouds and their shadows were masked out of the individual scenes before creating the image composites. Clouds and shadows were automatically detected using the Sen2Cor cloud detection algorithm (Louis et al., 2016). This method, however, generally shows high omission error rates for cloud shadows (Zhu and Woodcock, 2014). These undetected cloud shadows are often confused with water or wet surfaces, since these classes are spectrally very similar. A thorough cloud shadow removal is therefore essential to accurately map water and wetness. The Tmask algorithm proposed by Zhu and Woodcock (2014) yields better results for cloud shadow detection, but was discarded due to the required high computational effort.

Instead, a multi-temporal classification method based upon the time series of the NIR spectral band and the normalized differences between the blue, NIR, and SWIR1 channels was applied to mask out undetected cloud shadows. Using this method, pixels are classified as cloud shadows, if their NIR spectral value is lower than the 5th percentile of the time series and the normalized difference between the blue and the maximum of the NIR and SWIR1 bands is within the range of −0.25 and 0.25. Furthermore, cloud shadows are only flagged as such, if they are within a 20 pixel buffer around previously detected clouds. This approach is based upon two facts. First, shadowing leads to a strong decrease in reflectance of the NIR channel. Second, shadows have a flat spectral profile, so the normalized differences between all spectral bands is around zero.

2.3.1.2. Radiometric normalization. Prior to image compositing, all Sentinel-2 scenes were radiometrically normalized to one common reference image to reduce artifacts in image composites caused by differences in atmospheric conditions and solar illumination. The radiometric normalization was performed using histogram matching. The reference image for the normalization was derived by creating an image composite based upon the 25th percentile of all observations in the blue spectral band (see Section 2.3.1.3). The assumption behind this approach is that the 25th-percentile-composite will contain the clearest observations out of the whole time series thereby reliably excluding any form of atmospheric contamination that might impair the normalization result. An analysis of different reference images revealed that this method leads to the biggest decrease in Root Mean Square Error (RMSE) between the normalized images (Table 1). Histogram matching using these three reference images always led to a reduction of the RMSE in all bands compared to the original images. However, the seasonal reference image yielded the smallest improvement. This can be explained by the fact that even the best image within a season is more contaminated with clouds and shadows than the other two reference images. Using the best image of the whole time series yielded better results for most bands, but the smallest RMSE values were achieved using the 25th percentile composite.

2.3.1.3. Image compositing. Due to the frequent and high cloud coverage, especially in (sub-)tropical regions, single images do not always provide enough information to reliably delineate water and wetland extents throughout the year. Therefore, best pixel compositing was applied to create one continuous image for each month. In this way, seasonal bias due to higher cloud coverage during the rainy season in (sub)-tropical regions or the winter months in northern latitudes is avoided and spatially continuous water and wetness masks can be derived.

Various methods for image compositing exist. The most widely used method is the maximum value compositing procedure for which the pixel with the least probability for cloud and haze contamination is chosen for the composite depending on a certain criterion (Holben,

1986). Common criteria are the maximum NDVI, a minimum/maximum spectral value or a maximum ratio between two spectral bands (Gutman et al., 1994; Luo et al., 2008). Since all of these criteria have different strengths and weaknesses in excluding clouds and shadows from an image composite, Luo et al. (2008) and Lück and Van Niekerk (2016) proposed a combination of these criteria for image compositing using Landsat imagery. However, this method relies on the TCBI and Haze Optimized Transformation (HOT) which have not yet been adapted to Sentinel-2 imagery. Therefore, this method was not applicable in this study. The popular maximum NDVI compositing method is not suitable for wetland mapping, since it favours observations with high vegetation content over observations with high water or wetness content, which are typically characterized by low NDVI values. As a result, temporary occurrences of water or wetness are often excluded from the composite.

Instead, the 25th percentile of the blue spectral band of the whole image time series was used as the compositing criterion. This method is based upon the fact that the blue band is a good estimator of atmospheric contamination due to the high scattering effect in this spectral range. So it is assumed that the lower the reflectance value of the blue band, the less atmospheric contamination is present. Very low reflectance values, however, are often caused by shadows. Thus, creating a minimum blue composite might reliably exclude haze and clouds, but it will be very likely to include cloud shadows as well.

2.3.2. Spectral indices

A plethora of spectral indices has been used for open water and wetland mapping in past studies. Although many of these are good predictors for wetness, reliable wetness detection using a combination of indices from different scales was not possible. Combining indices of different scales poses the problem that the indices must be normalized prior to aggregation to weight every index equally. Depending on the normalization method, the original index value range that is sometimes connected to physical properties gets lost. This, however, is an important feature to ensure the selection of a valid threshold between water, wet and dry surfaces. To avoid this problem, the selection of indices was limited to Normalized Difference Indices (NDIs) as far as possible.

The most promising indices that were considered in this study are summarized in Table 2. To avoid confusion between the different NDWI definitions by McFeeters (1996) and Gao (1996), the latter one is hereinafter referred to as the Normalized Difference Moisture Index NDMI. Most of these indices are NDIs which are calculated using

$$ND_{B1B2} = \frac{B1 - B2}{B1 + B2} \quad (1)$$

where ND_{B1B2} is the resulting Normalized Difference Index based on bands B1 and B2. In this study, all NDIs were calculated in a way that high index values indicate high probability of water and wetness, while low values indicate dry land surfaces.

Due to the normalization, the value range of any NDI is [−1,1]. Therefore, these indices do not necessarily have to be normalized prior to water and wetness probability calculation (see Section 2.3.4) to make them comparable as it would be necessary, if indices of different scales were combined. The advantage hereof is that the physical meaning of the NDI is preserved in the probability index, e.g., a water probability value of 0.5 would correspond to a NDWI value of 0. This information can then be used in tile-based image thresholding to ensure the correct identification of valid thresholds (see Section 2.3.5).

To improve the detection of wetness over dense vegetation, additional indices had to be considered. The SASI is a spectral index that is sensitive towards changes in plant water content and soil moisture (Khannaa et al., 2007). It is, however, only defined for MODIS imagery. Das et al. (2017) proposed the Angle Based Drought Index 1 (ABDI1) and Angle Based Drought Index 2 (ABDI2) which are adaptations of the SASI for imagery that does not contain the same spectral bands as MODIS imagery. For Sentinel-2 imagery this yields two indices using SWIR1 for ABDI1 and SWIR2 for ABDI2. They were calculated using

$$ABDI = NIR \quad \arctan \frac{NIR - SWIR}{\lambda_{SWIR} - \lambda_{NIR}} \quad (2)$$

where SWIR and NIR are reflectance values and λ_{NIR} and λ_{SWIR} are the wavelengths of the respective bands.

2.3.2.1. Feature selection. For the identification of suitable index combinations to map water and wetness, feature selection analyses were performed based on the mutual information between the features and the class variable similar to Guo et al. (2008). Mutual information measures the dependence between two random variables and describes how much information they share. The higher the mutual information between an independent variable and a binary class variable such as water/non-water or wetness/non-wetness is, the closer the density distribution of the independent variable resembles a bimodal distribution. Maximizing mutual information between the independent variables and the class label will therefore yield an optimal bimodal distribution which is a key requirement for dynamic thresholding (Fig. 3).

The feature selection method proposed by Guo et al. (2008) is based on a consecutive selection of features based on mutual information yielding a feature ranking that gives an indication of the most important indices for water or wetness detection. The feature that shares the most information with the class variable is chosen as the first feature. For the selection of the subsequent features, the mutual information of each remaining feature with the class variable and the already selected features is calculated. In this way, subsequent features are chosen based on the additional information they contribute to the prediction of the class variable and not the absolute information shared with the class variable. As a result, features that are highly correlated with the already chosen features will be ranked lower, since they do not add much new information.

Feature rankings of indices were derived separately for each test site. First, the five most important indices were identified using the

Table 2
Spectral indices for water and wetness detection and their respective Sentinel-2 bands. Bands 8 and 8A can be used interchangeably.

Spectral index	Abbr.	Sentinel-2 bands	Reference
Normalized Difference Water Index	NDWI	B3, B8(A)	McFeeters (1996)
modified Normalized Difference Water Index	mNDWI	B3, B11	Xu (2006)
Normalized Difference Vegetation Index	NDVI	B4, B8(A)	Rouse et al. (1974)
Normalized Difference Moisture Index	NDMI	B8(A), B11	Gao (1996)
Normalized Multi-band Drought Index	NMDI	B8(A), (B11–B12)	Wang and Qu (2007)
Angle Based Drought Index 1	ABDI1	B8(A), B11	Das et al. (2017)
Angle Based Drought Index 2	ABDI2	B8(A), B12	Das et al. (2017)
Normalized Difference NIR - SWIR2	ND_{0812}	B8(A), B12	
Normalized Difference GREEN - SWIR2	ND_{0312}	B3, B12	
Normalized Difference SWIR1 - SWIR2	ND_{1112}	B11, B12	

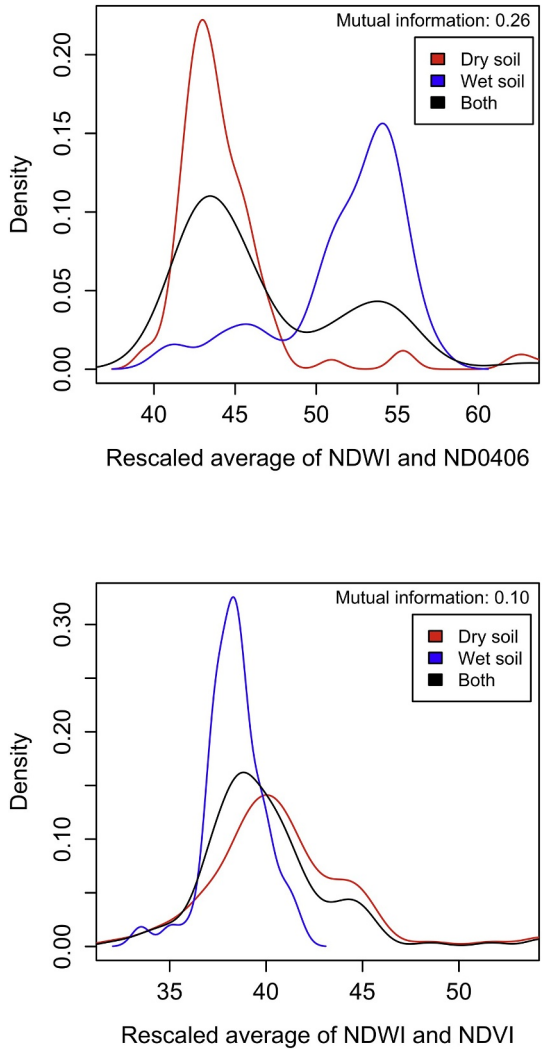

Fig. 3. Density distributions of different index combinations for dry and wet soil. Spectral index combinations that are suitable for the distinction between dry and wet soil show higher mutual information values and a bi-modal distribution (see details in text).

above described method. Subsequently, all possible combinations of two or three of these indices were calculated and mutual information between them and the class variable was calculated. Sorting them by mutual information, yielded a ranking of the best index combinations for each site. These results were taken as starting point to identify universally applicable index combinations for water and wetness detection.

The detectability of wetness strongly depends on the vegetation cover. Using only one index combination often leads to commission errors in urban areas or dry forests. Therefore, feature selection analyses were performed separately for bare soil (NDVI < 0.3), sparse vegetation (0.3 < NDVI < 0.6) and dense vegetation (0.6 < NDVI).

2.3.3. Topographic Wetness Index

Wetlands are easily confused with other upland land cover types such as forests, because these classes show overlapping spectral signatures (Ozesmi and Bauer, 2002; Tiner et al., 2015). Since the occurrence of wetlands and open water bodies strongly depends on the topographic conditions of a region, the TWI was included to improve classification results and reduce commission errors within upland areas. The TWI was defined by Beven and Kirkby (1979) as

$$\mathrm{TWI} = \ln\left(\frac{a}{\tan(b)}\right), \tag{3}$$

where a is the local up-slope contributing area draining through a point per unit contour length, and b is the local slope in radians. In flat areas, the TWI tends to unusual high value differences within a small distance introducing small artifacts (Buchanan et al., 2014). Therefore, a low-pass filter with a window size of 7 × 7 pixels was additionally applied to level out such irregularities.

For open water mapping, flood-prone areas were identified using the TWI. Water bodies that are detected outside this area are likely to be commission errors caused by shadows or other image artifacts. Therefore, only water bodies detected within the flood-prone areas were retained while others were reclassified to non-water.

The TWI was rescaled to a probability range of 0 to 1 and pixels with probability values above 0.5 were classified as flood-prone. This approach, however, tends to falsely exclude reservoirs built after the production date of the SRTM DEM. To avoid these omission errors, a water mask based on the median of mNDWI and NDWI of the whole time series was derived to identify such water bodies with high confidence. The TWI-derived flood mask was refined using this water mask with a 60 meter buffer, so that reservoirs are not falsely excluded from the detected water bodies.

2.3.4. Calculation of water and wetness probabilities

2.3.4.1. Water probability. The calculation of the water probability is based on a linear combination of spectral indices similar to a regression analysis. However, the assumption behind this calculation is that all indices share the same value range and that high index values indicate a high water probability with a high contrast between flooded and non-flooded areas. To assure the first assumption, all indices are rescaled to a value range of 0 to 1 prior to calculation. The water probability was calculated using

$$P_{water} = \sum_{i=1}^{n} w_i u_i \tag{4}$$

where P_{water} is the probability that a pixel belongs to the class water, u_i are values of spectral indices for water detection and w_i the weight of the respective index. In contrast to a regression analysis, all weights were set to $1/n$ to remove the need for training data. This is sufficient, since the contrast between water and non-water areas is usually high and the adaptation of the water detection algorithm to different local conditions can be performed in a robust way using the dynamic thresholding algorithm (see Section 2.3.5).

2.3.4.2. Wetness probability. The spectral signature of wet surfaces is highly dependent on the vegetation cover, thus, three different wetness probabilities quantifying the presence of wetness over bare soil (NDVI < 0.3), sparse vegetation (0.3 < NDVI < 0.6) and dense vegetation (NDVI > 0.6) were calculated. All of these wetness probabilities were calculated in the same way, but using different spectral indices that are sensitive to wetness above the respective vegetation cover type. The derivation of the wetness probability is based on spectral and topographic data and is calculated using

$$P_{wet} = \sigma\left(\sum_{i=1}^{n} w_i v_i\right) \times (\sigma(TWI)\beta + \alpha), \tag{5}$$

where P_{wet} is the probability that a pixel belongs to the class wetness, v_i are values of spectral indices, w_i the weight of the respective index, *TWI* is the Topographic Wetness Index, α and β are coefficients for linear scaling of the TWI and σ is a sigmoid function defined as

$$\sigma(x) = \frac{1}{1 + e^{-x}}, \tag{6}$$

The first term of Eq. (5) represents the spectral wetness information,

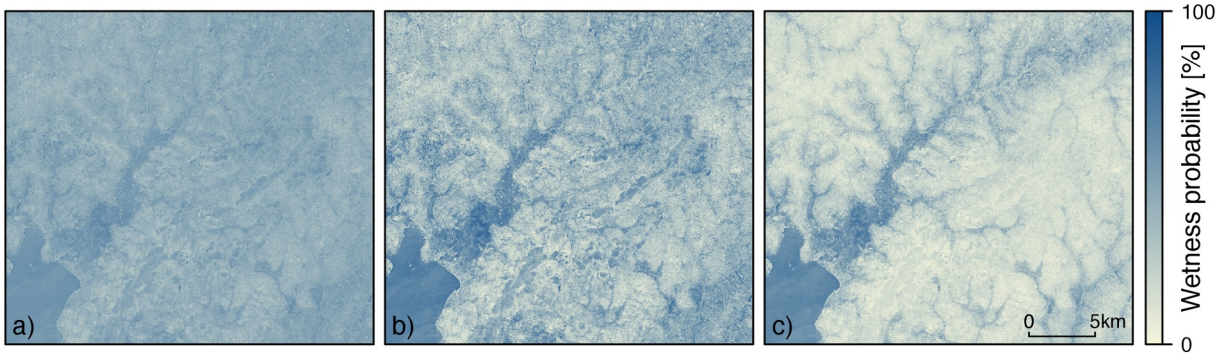

Fig. 4. The wetness probability calculation involves three steps which successively increase the contrast between wet and dry areas: (a) Spectral indices sensitive to wetness are linearly combined; (b) the result is transformed using a sigmoid function; (c) the contrast is further increased by weighting the result using the TWI.

which is also based on a linear combination of spectral indices with the same assumptions as for water detection, so all indices share the same value range and high index values indicate high wetness levels. However, since the spectral contrast between wet and dry surfaces is not as pronounced as for open water (Fig. 4a), additional image enhancement methods were incorporated into the calculation of the wetness probability to increase the separability of the classes without the usage of training data. First of all, each wetness index was linearly scaled to a value range of [0,1] using the 1st and 99th percentile of the complete index time series excluding open water areas. The 1st percentile can be interpreted as the driest pixel found in the time series, while the value at the 99th percentile represents the wettest pixel. By scaling the index using these boundaries, image contrast is increased and the density distributions of the indices are better aligned to form an optimal bimodal distribution which is an important precondition for the dynamic thresholding algorithm. Deriving the boundary values based on the complete times series instead of the respective image preserves the common scale of the monthly indices, so that the values of the minimum threshold introduced from dynamic thresholding are suitable for all image composites. As in logistic regression, the linearly combined indices are transformed using a sigmoid function to further enhance the contrast in the transition zone from dry to wet resulting in a better separability of the two classes in the final wetness probability image (Fig. 4b).

The second term of Eq. (5) represents the topographic part of the wetness probability calculation. The main purpose of weighting the spectral wetness probability with the topographic information is to reduce commission errors within upland forests by decreasing the wetness probability in non-flood prone areas (Fig. 4c). The sigmoid function reduces the roughness of the TWI values in flat areas, where the TWI sometimes shows unusual artifacts (Buchanan et al., 2014). The TWI is furthermore scaled to a value range of [0.75, 1] using $\alpha = 0.75$ and $\beta = 0.25$ to limit its influence on the wetness probability value so that the dynamics of the seasonally changing spectral indices is preserved. Different scaling ranges where tested, but this one gave the best results by balancing preservation of seasonality and reduction of commission errors.

2.3.5. Tile-based image thresholding

A tile-based image thresholding similar to Martinis et al. (2009), which is a modified version of the original Otsu thresholding (Otsu, 1975), was used to successively derive the extent of water and wetness areas for each monthly composite. Otsu thresholding is a method in image processing that is used to reduce a grey level image to a binary image (Otsu, 1975). Using the original Otsu method, the optimal threshold is identified by minimizing the inter-class variance and maximizing the intra-class variance. For this purpose, however, this method did not yield satisfying results. Instead, the threshold was identified by searching for the minimum in the density distribution. In case several local minima were detected, the most pronounced minimum between two peaks providing the largest fraction of area under the density distribution function was chosen.

In tile-based image thresholding, the image is first divided into equally sized quadratic tiles. The thresholding is subsequently only applied to those tiles with the highest variances (larger than 95th percentile) to derive a local threshold for each tile. The variance is hereby used as an indicator for the probability that the tile contains sufficiently large fractions of both classes to guarantee that a valid threshold can be derived. The mean or median of all local thresholds is calculated to get a global threshold. In the original approach proposed by Martinis et al. (2009), this global threshold is applied to the whole image to derive a binary classification result. Herein, the global threshold based on the median was adapted for each tile by weighting it with the mean of the neighboring local thresholds. In this way, the edges of water bodies are captured more accurately while still retaining a homogeneous water mask.

The calculation of the local thresholds can be controlled by the tile size and the minimum threshold value. The selection of the tile size depends on the spatial resolution of the image and the distribution of the two classes within the image (Martinis et al., 2009). When applying Otsu thresholding, a valid threshold can only be derived if both classes cover roughly equal portions of the image to get a bimodal density distribution. Dividing the image into very small tiles increases the processing time and the likelihood that tiles are included in the threshold calculation which do not include the transition zone between the two classes. If the tile size is too large, the area fraction of either of the two classes is too small to form a bimodal distribution.

An analysis of different tile widths from 20 to 200 pixels showed that the tile size for water and wetness detection using Sentinel-2 imagery should be at least 50 × 50 pixels to derive valid thresholds. For tile sizes bigger than this, the derived thresholds tend to stabilize with minor fluctuations. For the three study sites, the tile size was kept at a constant value of 90 × 90 pixels.

Undetected clouds in satellite imagery often lead to omission errors above water bodies. To reduce these, a minimum water mask representing the permanent water bodies in the scene was derived using the 10th percentile of the mNDWI and NDWI time series. In this way, omission errors in the monthly water masks were reclassified to water.

The split-based image thresholding sometimes leads to the identification of wrong thresholds, if the contrast between the two classes is not strong enough or one of the classes is not present in the image at all. As a result, the derived water or wetness probability threshold might be invalid, e.g., it separates dry from wet surfaces instead of water from land (Fig. 5). To increase the robustness of the method with regard to these kinds of errors, constraints to the dynamic thresholding algorithm were introduced in the form of minimum water and wetness probability thresholds. Local thresholds that are lower than the specified minimum are not considered for the calculation of the final global threshold that

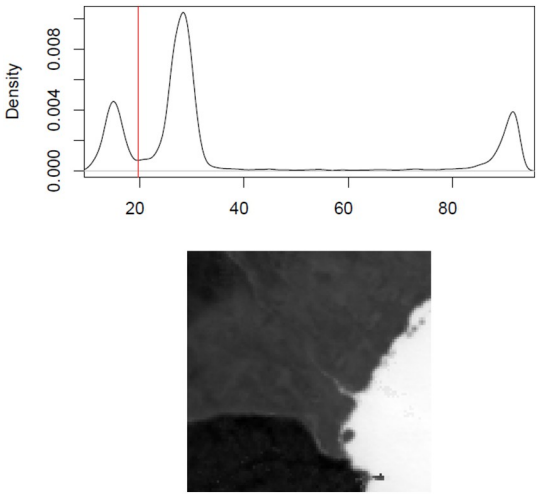

Fig. 5. At the bottom, image tile showing the water probability (scaled to [0,100]). On top, the respective histogram with the falsely detected threshold marked in red, if no minimum water probability threshold is set. In this case, the true threshold separating water and land should be between 40 and 80% water probability. (For interpretation of the references to color in this figure legend, the reader is referred to the web version of this article.)

is applied to the whole image. Adjusting this parameter to the single study sites reduces the number of falsely detected thresholds making the derivation of the true threshold more reliable and robust.

2.3.6. Wetland classification

The frequencies for water and wetness over the whole observation period are calculated separately based on the binary masks. Note here that all water and wetness classes are mutually exclusive for each observation. Since the contrast between water and non-water is higher than the contrast between wet and dry surfaces, water detection is performed first. Pixels that have been classified as water in the first step, are excluded from the subsequent wetness detection. The three wetness classes are also mutually exclusive, since they are applied to different areas based on the NDVI thresholds (see Section 2.3.4.1). In this way, it is ensured that the water, wetness and dryness frequencies sum to unity.

To avoid seasonal biases due to differences in cloud coverage during the year, the frequencies were calculated separately, but using the same formula

$$f_{ij} = \frac{1}{s}\sum_{k=1}^{s}\frac{1}{n_s}\sum_{t=1}^{n_s} c_{ij}^{t}, \tag{7}$$

where f_{ij} is the overall water or wetness frequency for a pixel at location ij, s is the number of seasons, n_s is the number of valid observations for pixel ij within season s, c_{ij}^{t} is the binary class value of the pixel ij at observation t, where 0 represents non-water/non-wetness and 1 represents water/wetness. Seasons were defined as three monthly periods, therefore s was set to 4.

The Water Wetness Presence (or Probability) Index WWPI, as defined by the EEA Copernicus Land Monitoring Service, gives an indication of the occurrence of water and wetness within the investigation period. The WWPI ranges from 0 to 100% and is calculated using

$$\mathrm{WWPI} = \frac{\sum water + 0.75\sum wet}{n}*100, \tag{8}$$

where $\sum water$ is the number of water occurrences per pixel, $\sum wet$ is the number of wetness occurrences per pixel and n the number of valid observations per pixel. The classes water, wet and dry are mutually exclusive meaning that a pixel can only belong to one class at a certain point in time. Therefore, the WWPI ranges from 0 (always dry) to 100% (always flooded). The weighting factor 0.75 was defined according to Langanke et al. (2016), but was not empirically derived within this study.

The main outcome of the proposed approach are water, wetness, and dryness frequency maps as well as the WWPI. These layers indicate where wetlands are likely to occur and thus serve as a pre-inventory. Applying a rule-based classification, these layers can be translated into wetland information, which has been done in the context of the Copernicus HRL Water and Wetness Layer (Langanke et al., 2016).

2.3.7. Product validation

The validation of a multi-temporal product is challenging using single-date reference data. Therefore, water and wetness masks derived from two monthly composites of each site were validated to get an estimation of the classification accuracy.

The accuracy assessment was implemented according to the good practice recommendations of Olofsson et al. (2014). Stratified random sampling was chosen as sampling design to create validation points within the three strata water, wet and dry areas. The number of sample points was not allocated purely proportionally to the size of the strata to balance the precision of user's, producer's and overall accuracy (Olofsson et al., 2014). The class with the largest area fraction (dry areas) was assigned 350 sample points, for each of the classes water and wet 100 sample points were assigned which resulted in a total of 550 samples per site and season. The validation was done blind, thus, the validator had no information about the classification results. The reference data for the validation included Google Earth Imagery, Open Street Map data as well as the respective monthly image composite and the derived NDWI and mNDWI images to get an indication of the current water and wetness presence.

The accuracy of each monthly water and wetness classification is describe using an error matrix and the derived accuracy parameters overall, user's and producer's accuracy (Olofsson et al., 2014). The sampling variability is quantified by the 95% confidence interval (CI). In addition, the kappa coefficient of agreement was calculated for each accuracy assessment (Congalton and Green, 2008).

3. Results

3.1. Feature selection analysis

3.1.1. Water

Initially, the mNDWI, NDWI, and NDVI were taken into consideration for water detection, as these indices have already been proven suitable for this purpose in previous studies (Li et al., 2013; Chen et al., 2013; Rokni et al., 2014; Jiang et al., 2014; Tetteh and Schönert, 2015; Donchyts et al., 2016). Different single and multi-index configurations were tested. Using NDWI for water detection led to commission errors within urban areas, while mNDWI tended to confuse wet soil and open water in dry, sandy regions (Fig. 5). Adding the NDVI to one of these water indices reduced detection rates over water bodies that contained some form of vegetation. In the end, the combination of mNDWI and NDWI yielded the most reliable and accurate results by combining the advantages of both indices. The contrast between water and land is increased and commission errors within urban areas are reduced. The suitability of this index combination was also compared to other indices using the feature selection analysis based on mutual information, but none of the other index combination performed significantly better. In addition, water probability calculation is very straight forward using mNDWI and NDWI, since they are both NDIs which makes rescaling unnecessary. The general applicability of this index combination also proved to be very high, since the minimum water probability value was kept at 50% for all study sites (Table 3).

3.1.2. Wetness

To identify suitable index combinations for wetness detection,

Table 3
Spectral indices used for water and wetness detection and respective minimum water and wetness probability values of each study site.

Class	Indices			Minimum probability [%]		
				Algeria	Uganda	Austria
Open water	NDWI	mNDWI		50	50	50
Bare soil	ND_{0812}	NDWI	ND_{0312}	55	50	50
Sparse vegetation	ND_{0812}	NDWI	NMDI	55	45	50
Dense vegetation	ND_{0812}	ABDI1	ABDI2	60	60	65

feature selection analyses were performed separately for each study site. The resulting feature rankings were analyzed jointly to find suitable index combinations that are applicable for wetness detection in a generic manner within a broad range of bio-geographical regions. Three different index combinations were identified that are sensitive to wetness among different degrees of vegetation cover (Table 3).

The Normalized Difference Index between the NIR and SWIR2 bands (ND_{0812}) is present in each of them, since it was ranked as a very important index in all feature rankings and across all study sites. This selection is plausible, since different combinations of NIR and SWIR bands have been used for wetness detection in many previous studies due to their sensitivity towards changes in soil moisture and plant water content, e.g., SASI (Khannaa et al., 2007) and NDMI (Gao, 1996).

For wetness detection over bare soil, the ND_{0812} was supplemented with the NDWI and ND_{0312}. This index combination is mainly focused on the detection of very wet or slightly inundated soils that were not classified as open water due to the mixed pixel effect. These areas are mainly found along narrow rivers, shorelines and shallow lakes and marshes such as the Marais de la Mekhada in Algeria or the Sio River (Fig. 6). The spectral profile of these land surfaces is very similar to open water but less pronounced. Therefore, typical water indices such as the NDWI and ND_{0312} are also suitable for wetness detection within these land cover types. The minimum wetness probability value for this index was mostly kept at 50%. For the study site in Algeria, it was slightly increased by 5% to reduce the amount of commission errors (Table 3).

The main challenge for the detection of wetness within densely vegetated areas is to differentiate dry upland forests from forested wetlands and peatlands such as the Oum Lâagareb wetland in Algeria. The inclusion of the TWI in the calculation of wetness probabilities eliminates most upland forests, but not entirely. Therefore, the separability between these two classes has to be enhanced by including spectral indices that quantify differences in leaf water content. The feature selection clearly showed that ABDI1 and ABDI2 are the most suitable indices to achieve this, since they are sensitive to plant water content and drought stress. The minimum probability values of this class were generally set to a higher value than the others ranging between 60 and 65% to reduce commission errors within dry forests.

The identification of a suitable index combination for wetlands with sparse vegetation was especially relevant for the Sio-Siteko Wetland, since the other two index combinations were not sensitive towards the central region of the wetland (Fig. 6). The feature selection analysis identified the NMDI as the most important index which was then

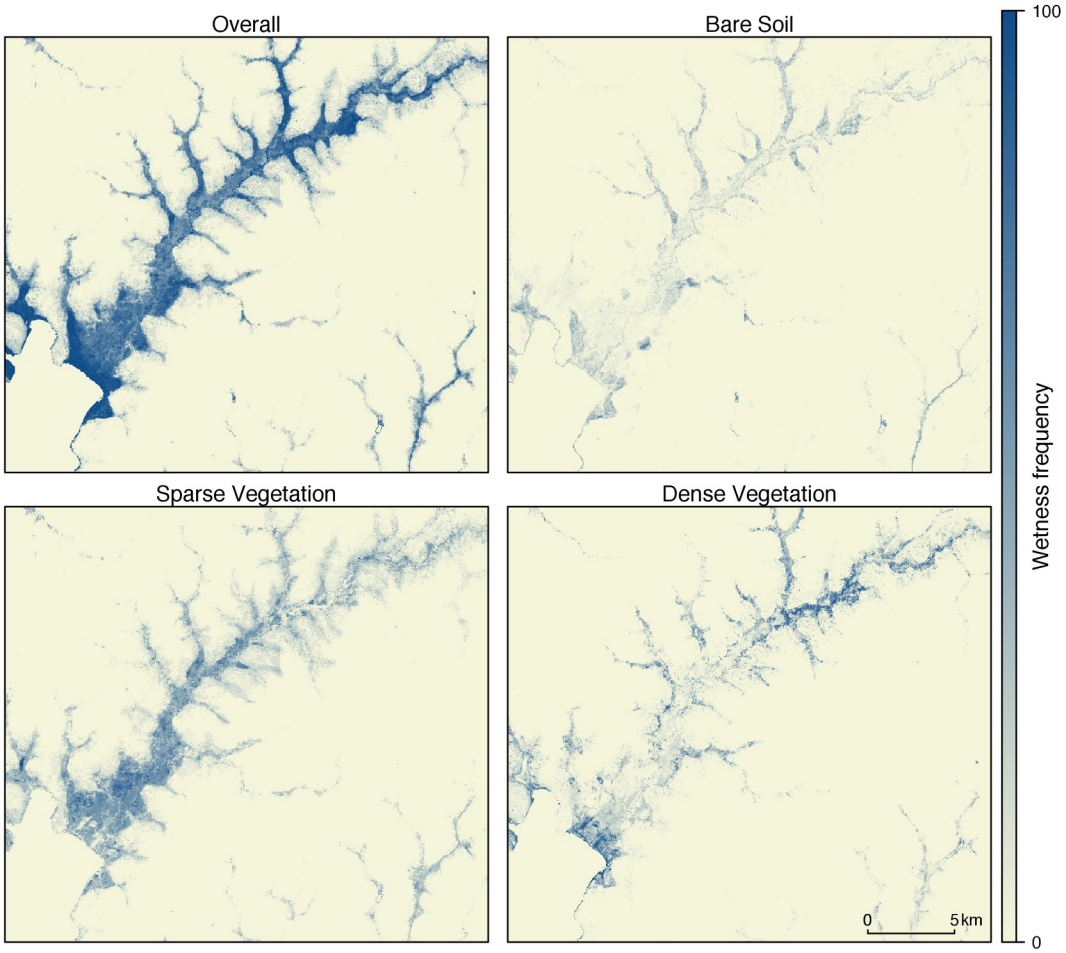

Fig. 6. Sio-Siteko Wetland, Site A: Wetness frequencies over bare soil, sparse vegetation and dense vegetation derived using the spectral indices shown in Table 3. The sum of these frequencies gives the overall wetness frequency.

Table 4
Accuracy assessment for El-Kala Wetland System in February 2016.

Classification	Reference			Total	User's acc.	95% CI
	Dry	Water	Wet			
Dry	325	0	25	350	92.86	1.45
Water	0	97	3	100	97.00	1.73
Wet	10	1	89	100	89.00	3.46
Total	335	98	117	550		
Prod.'s acc. [%]	97.01	98.98	76.07			
95% CI	0.94	1.01	5.10			
Overall acc.	92.91%					
Overall 95% CI	1.16					
Kappa	0.87					

supplemented with ND_{0812} and NDWI. The spectral profile of wetlands within this class is heterogeneous depending on the ratio between bare soil and vegetation. Therefore, the applied minimum wetness probability value for this class varies slightly more within the study sites than the other index combinations ranging between 45 and 55%. In Uganda, it was set to a rather low value to reduce omission errors within the central part of the wetland, while for the other sites it was set to a higher value to keep commission errors low.

3.2. El-Kala Wetland System, Algeria

The accuracy assessment for the El-Kala Wetland System was performed for February 2016 (Table 4) and June 2017 (Table 5). Both show overall accuracies over 92 %. Water was more accurately mapped reaching producer's and user's accuracy values exceeding 96% an 97%, respectively. There is minor confusion between wet soil and water within the Marais de la Mekhada due to the shallow water which makes the distinction using visual interpretation difficult. Accuracy levels for wetness reach producer's and user's accuracy of at least 76% and 89%, respectively, with most misclassifications occurring within agricultural fields.

The WWPI gives a good representation of the spatial distribution of water and wetness in the area around the El-Kala Wetland System (Fig. 7). The floodplain including the Marais de la Mekhada as well as Lake Oubeira and Lake Tonga in the East show high WWPI values, while the surrounding upland areas are permanently dry. Several agricultural fields which are partly irrigated during the growing season are scattered throughout the valleys showing medium high WWPI values. Urban areas are reliably classified as dry showing very few commission errors. Minor commission errors only occur within the dry forest near the shore. Permanent water bodies and the ocean have been delineated accurately showing no omission errors. Especially the smaller water reservoirs have been mapped with high reliability.

Table 5
Accuracy assessment for the El-Kala Wetland System in June 2017.

Classification	Reference			Total	User's acc. [%]	95% CI
	Dry	Water	Wet			
Dry	339	0	10	349	97.13	0.90
Water	0	99	0	99	100.00	0.00
Wet	1	4	95	100	95.00	2.26
Total	340	103	105	548		
Prod.'s acc. [%]	99.71	96.12	90.48			
95% CI	0.29	1.95	3.12			
Overall acc.	97.26%					
Overall 95% CI	0.70					
Kappa	0.95					

The seasonal wetness frequencies over dense vegetation reflect the seasonal presence of agriculture in the floodplain and the forested swamps of Oum Lâagareb (Fig. 8). During the growing season in winter and spring the flood plain shows high wetness frequencies due to irrigation of agricultural areas. In summer, the flood plain is dry and no longer vegetated. Only the forested swamps of Oum Lâagareb in the North West appear as wet. During fall, moisture levels seem to drop in this area as well.

Due to the dry summers and rainy winters, water and wetness occurrence are considerably reduced in summer (Fig. 9). The water within the Marais de la Mekhada recedes, but the marsh stays moist while the surrounding area is dry. In winter, the marsh is flooded reaching its maximum water extent and the whole flood plain shows generally high moisture levels due to agricultural activity. This corresponds to the seasonal distribution of precipitation, since rainfall mainly occurs in winter and agricultural fields within the flood plain are irrigated during the growing season in winter and spring.

Lake Tonga shows a similar pattern (Fig. 10). During winter, the water level is highest and most of the surface is flooded. In summer, the water level drops, but the vegetation covering the lake seems to retain some level of moisture throughout the whole year. The agricultural fields in the south-east of the lake also show the typical seasonal dynamics with high wetness occurrence in winter and dryness in summer.

3.3. Sio-Siteko Wetland, Uganda/Kenya

For the Sio-Siteko wetland, the water and wetness extents for August (Table 6) and December 2016 (Table 7) were validated. Overall accuracies are high with values of 92% and 95%, and kappa coefficients of 0.87 and 0.85. Water was detected very well with both user's and producer's accuracy reaching 100%. User's accuracy of wetness in April only reaches 65% with most commission errors located within agricultural fields. In December, the user's accuracy reaches 86%. Producer's accuracy is satisfying in both months reaching more than 86%. The omission errors are mostly found at the edges of the wetlands or within small wetland patches.

The WWPI delineates Lake Victoria and the branches of the wetland system accurately (Fig. 11). The wetland shows constantly high WWPI values which seems plausible given the tropical climate. Agricultural areas that are located along the edges of the wetland branches are also visible with medium WWPI values.

The water level of Lake Victoria does not vary considerably during the year, which can be seen by constantly high WWPI values. The Sio river that flows through the Sio-Siteko main wetland (Fig. 11A) was not classified as water, since in most parts the width is smaller than the 20 m spatial resolution of the imagery. The importance of using different spectral indices for different degrees of vegetation cover can be seen very clearly in the Sio-Siteko main wetland branch (Fig. 6). The densely vegetated swamps in the northern and southern part of the wetland are well captured by the drought indices ABDI and the ND_{0812}. The central part of the wetland is generally less vegetated, which makes the drought indices less suitable for wetness detection. The NMDI, on the other hand, is very sensitive towards wetness in this area, yielding high wetness frequency values in the sparse vegetation map. The wetness frequency over bare soil mainly captures less vegetated areas that are sightly flooded or rivers that are too narrow to be classified as water such as the Sio river.

The Nzoia River and its flood plain south of Sio-Siteko shows seasonal water level changes (Fig. 12). While the river permanently contains water, cut-off meanders and rice paddies within the floodplain are only seasonally flooded. Some segments of the river show reduced water frequency values, which are often due to omission errors caused by turbid water, vegetation cover or narrow river width. These areas are captured by the bare soil wetness detection. The presence of

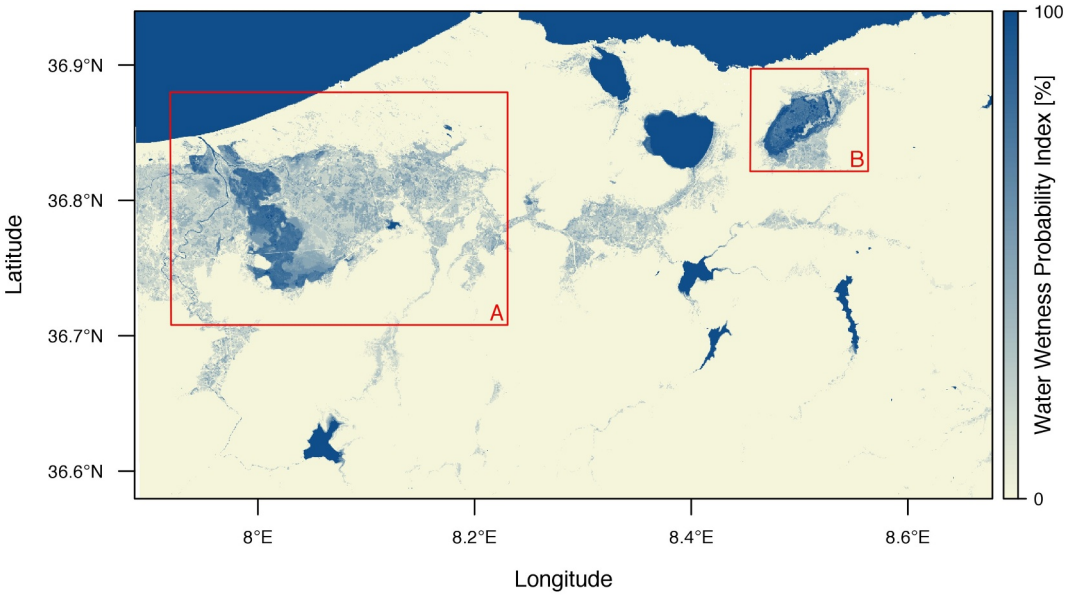

Fig. 7. El-Kala Wetlands: WWPI (Jan 2016–June 2017). Site A is the Marais de la Mekhada, a freshwater marsh in the Mafragh plain and site B is Lake Tonga.

wetness also seems plausible with the rice paddies and swamps being frequently wet while the upland regions and the urban settlements are classified as mostly dry.

3.4. Lake Neudsiedl, Austria

The water and wetness classification for April 2016 (Table 8) and August 2016 (Table 9) were validated. The accuracy assessment yields overall accuracies in both cases of 93% and 92%, respectively. Water was detected very accurately in both months. For wetness, producer's accuracy reaches values of at least 86%. Due to omission errors on the edges of the reed belt of Lake Neusiedl, the producer's accuracy is decreased.

The WWPI shows high values throughout Lake Neusiedl and its surrounding marsh land (Fig. 13). The area east of the lake is extensively farmed and irrigated at times, which explains the increased WWPI outside of the wetland. The surrounding upland forests and urban settlements are mostly classified as dry showing only minor commission errors.

The changing water level of Lake Neusiedl and its surrounding marsh land are well captured in the annual water frequency map (Fig. 14c). While the water level of the lake remains relatively constant throughout the year, the smaller lakes in the surrounding area show strong fluctuations. Some of these lakes even disappear completely

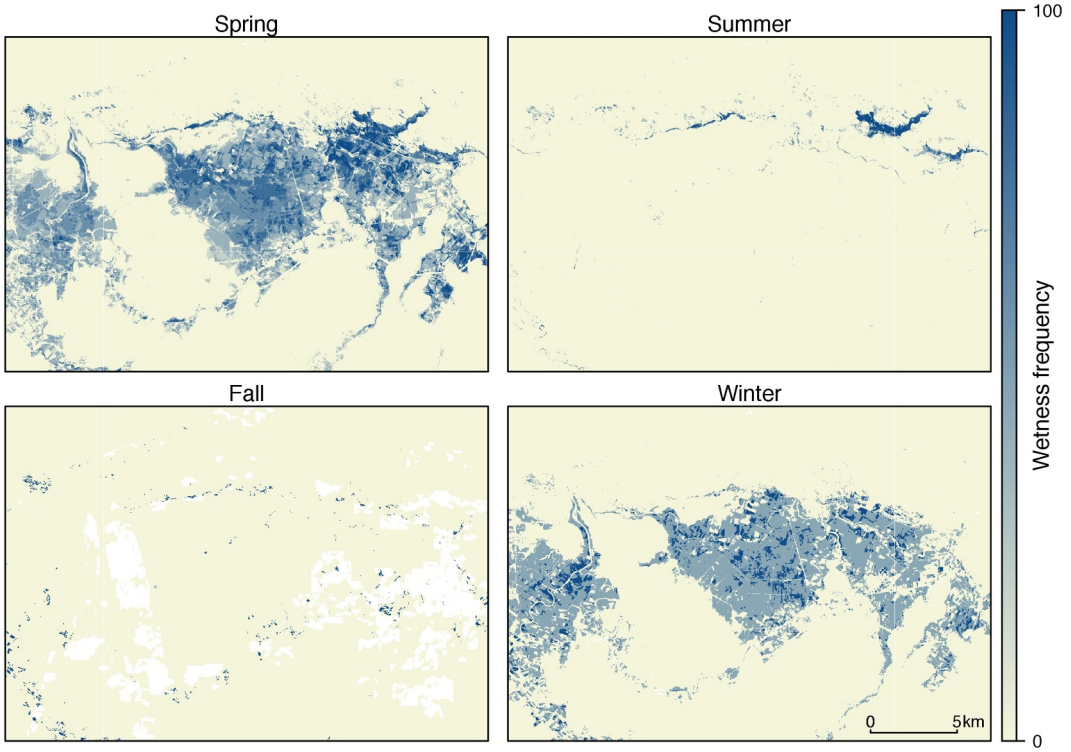

Fig. 8. El-Kala Wetlands, Site A: Seasonal wetness frequency for dense vegetation (Jan 2016–June 2017). White areas represent no data.

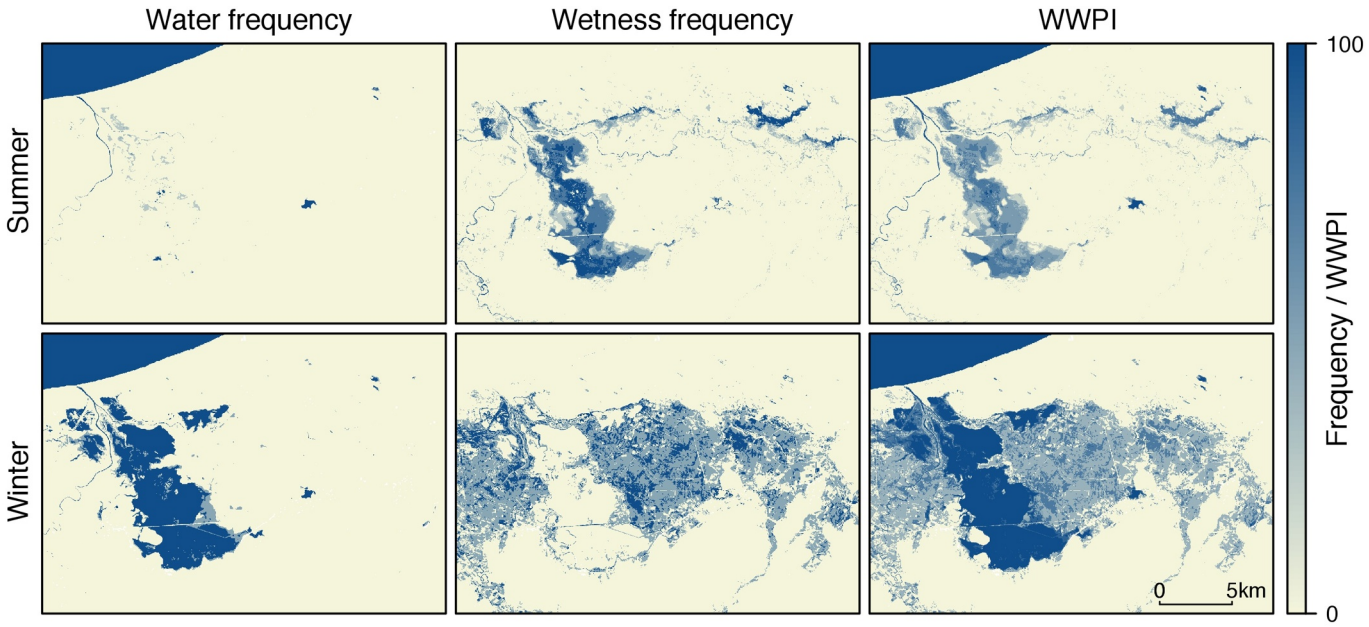

Fig. 9. El-Kala Wetlands, Site A, Marais de la Mekhada: Water and wetness frequency and WWPI for summer and winter (Jan 2016–June 2017).

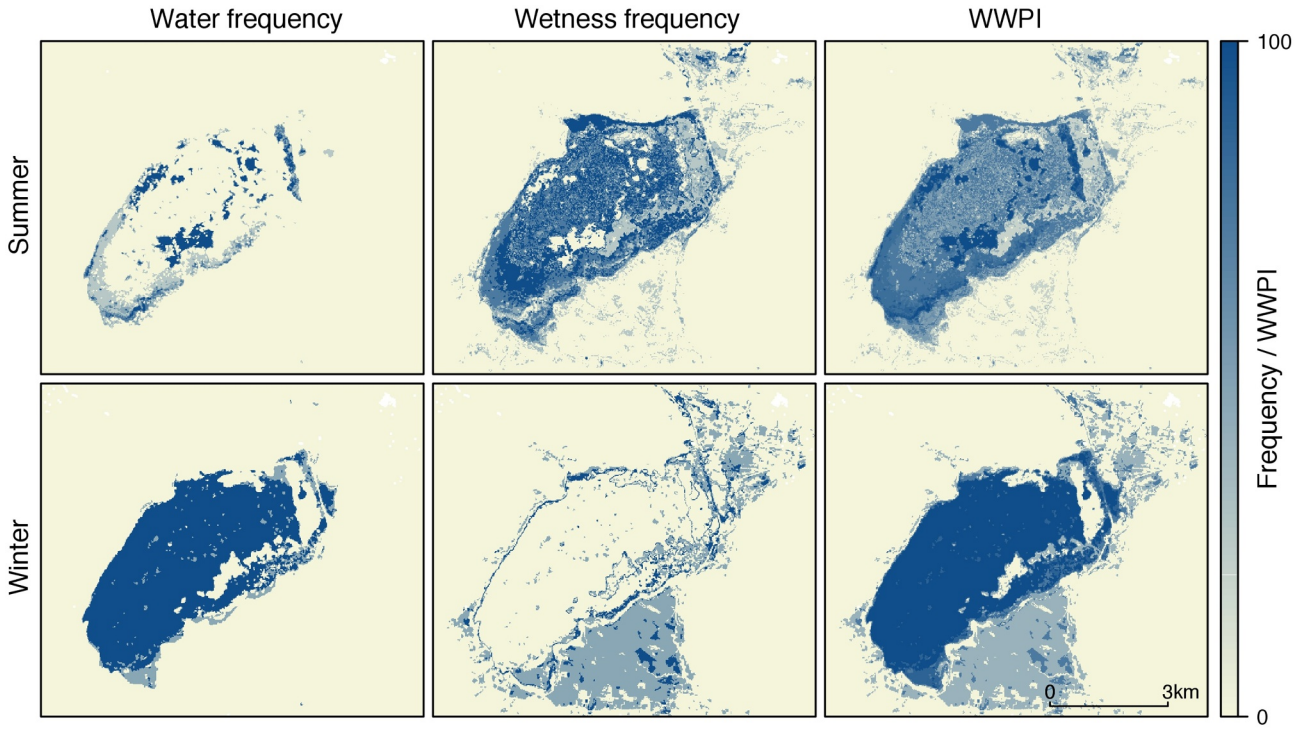

Fig. 10. El-Kala Wetlands, Site B, Lake Tonga: Water and wetness frequency and WWPI for summer and winter (Jan 2016–June 2017).

during the summer months. The seasonal wetness frequency also reflects the changing moisture level of the reed belt surrounding the lake. The highest wetness frequencies are reached during the rainy winter months, while areas around the edges of the marsh dry out considerably during the summer (Fig. 14b,c). Large parts of the area around Lake Neusiedl are used for agricultural purposes, which is why these fields temporarily show high wetness frequencies. Some forested patches within the agriculturally used south-eastern part of the site show wetness frequency value of up to 60% which probably constitute errors of commission, but might also be due to a high plant water content.

4. Discussion and conclusion

The aim of this study was to investigate whether wetland mapping can be performed in large areas and across different bio-geographic regions in a highly automated way and without the need for extensive training data. For this purpose, a method based on tile-based image thresholding to semi-automatically map water and wetness using multi-temporal optical satellite imagery was developed and evaluated. Feature selection analyses were performed using the mutual information criterion to find combinations of spectral indices that are suitable

Table 6
Accuracy assessment for Sio-Siteko Wetland in August 2016.

Classification	Reference			Total	User's acc.	95% CI
	Dry	Water	Wet			
Dry	341	0	8	349	97.71	0.80
Water	0	100	0	100	100.00	0.00
Wet	35	0	65	100	65.00	7.23
Total	376	100	73	549		
Prod.'s acc. [%]	90.69	100.00	89.04			
95% CI	1.62	0.00	4.05			
Overall acc.	92.17%					
Overall 95% CI	1.22					
Kappa	0.85					

Table 7
Accuracy assessment for Sio-Siteko Wetland in December 2016.

Classification	Reference			Total	User's acc.	95% CI
	Dry	Water	Wet			
Dry	337	0	13	350	96.29	1.03
Water	0	100	0	100	100.00	0.00
Wet	13	0	85	98	86.73	3.89
Total	350	100	98	548		
Prod.'s acc. [%]	96.29	100.00	86.73			
95% CI						
Overall acc.	95.26%					
Overall 95% CI	0.94					
Kappa	0.91					

for water and wetness detection in different bio-geographical regions. The method was applied to three study sites covering different climatic regions to evaluate its performance and degree of general applicability.

The results prove that tile-based image thresholding is an effective and fast method to map water and wetness in an mostly automatic way. The validation of selected monthly water and wetness extents yielded satisfying results reaching overall accuracies of at least 92% for all test sites. Moreover, plausibility checks using climate data and site descriptions by Ramsar indicate that the derived classifications seem to convey a plausible representation of water and wetness occurrence throughout the year. Comparisons of the annual water frequencies derived for the three study sites to the Global Surface Water data set by Pekel et al. (2016) revealed good concordance, which supports the plausibility and accuracy of the classification. In the case of Lake Tonga, both classifications exhibit the same patterns, but the classification derived in this study results in generally higher water frequencies within the lake (Fig. 15). This seems to be plausible, since the lake is permanently flooded and partly covered by floating vegetation (Fig. 15). For the whole study site in Algeria, the mean difference between the two water frequencies was 0.2% with a standard deviation of 7.0%. However, the significance of this comparison is limited due to the differences of the satellite sensors, investigation periods and temporal resolution for both products which may account for some of the deviations between the two classification results. Considering wetness, there is no such reference available, which is why plausibility was tested using climate data. Those comparisons, however, indicated that the changing extents of wet surfaces generally corresponded to the annual rainfall distribution for both study sites.

Open water was very accurately mapped with user's and producer's accuracies exceeding 96% for all test sites. Limitations arise in narrow streams with turbid water or dense vegetation cover, because mixed pixels complicate water detection. Fusing the optical-based water masks with water masks derived from Sentinel-1 improves detection

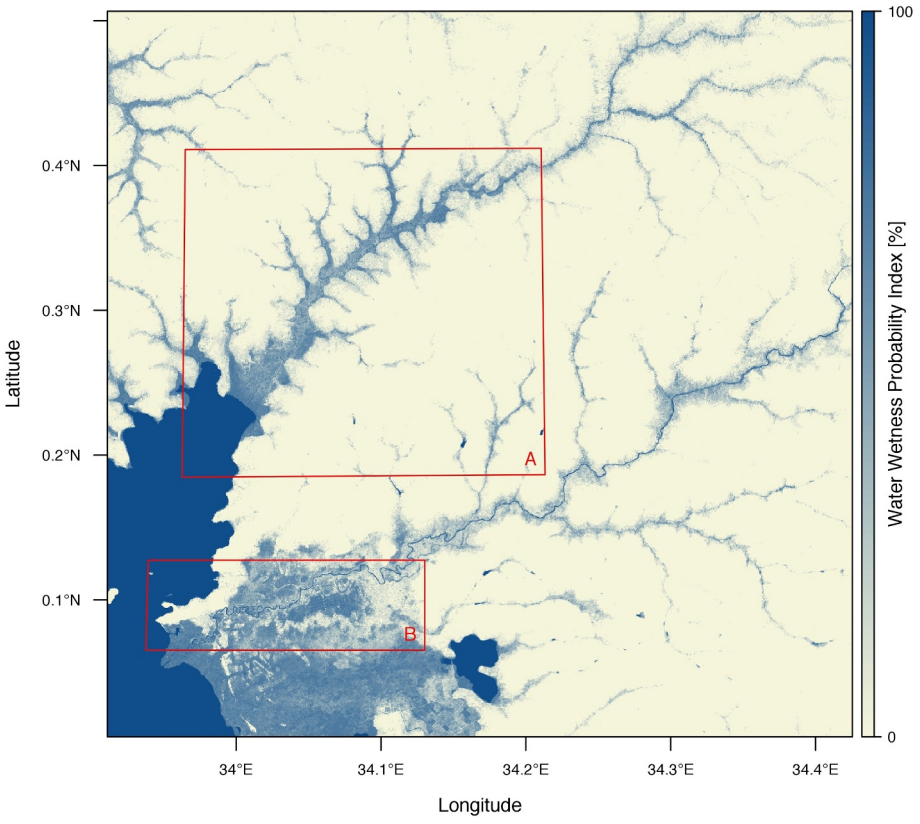

Fig. 11. Sio-Siteko Wetland: WWPI (Jan 2016–June 2017). Site A is the Sio-Siteko Wetland and Site B is the Nzoia River.

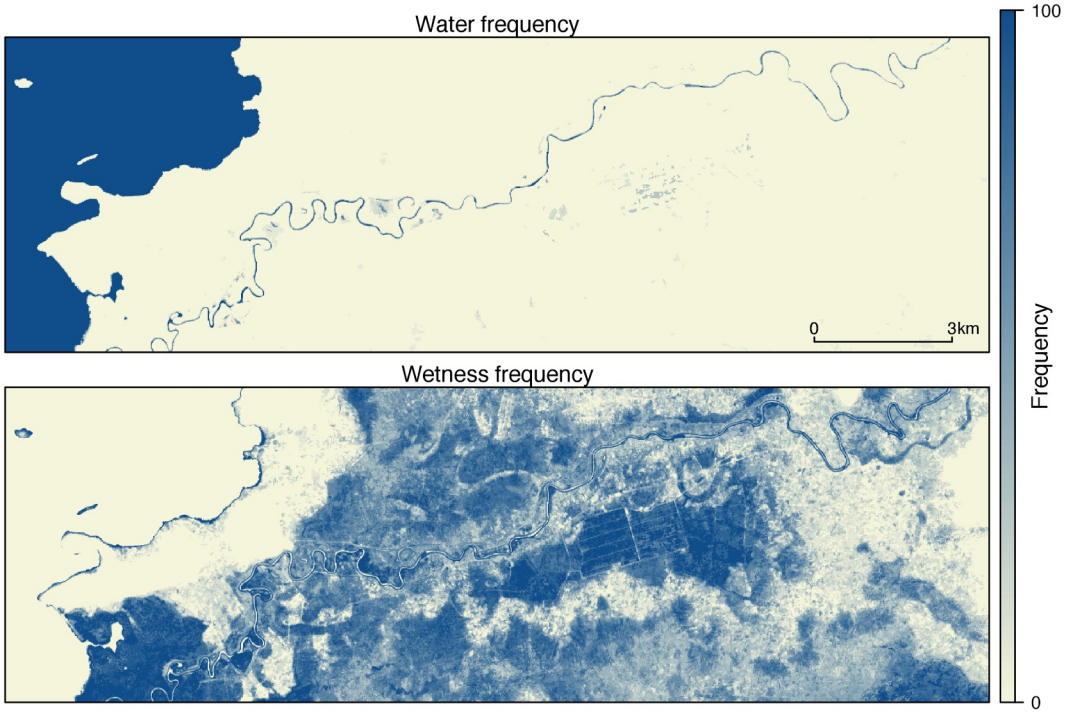

Fig. 12. Sio-Siteko Wetland, Site B, Nzoia River: Water and wetness frequency of the Nzoia River.

Table 8
Accuracy assessment for Lake Neudsiedl in April 2016.

Classification	Reference			Total	User's acc.	95% CI
	Dry	Water	Wet			
Dry	323	0	25	348	92.82	1.46
Water	0	100	0	100	100.00	0.00
Wet	11	2	87	100	87.00	3.81
Total	334	102	112	548		
Prod.'s acc. [%]	96.71	98.04	77.68			
95% CI	0.99	1.38	4.99			
Overall acc.	93.07%					
Overall 95% CI	1.14					
Kappa	0.87					

Table 9
Accuracy assessment for Lake Neudsiedl in August 2016.

Classification	Reference			Total	User's acc.	95% CI
	Dry	Water	Wet			
Dry	316	0	30	346	91.33	1.63
Water	0	98	0	98	100.00	0.00
Wet	13	0	85	98	86.73	3.89
Total	329	98	115	542		
Prod.'s acc. [%]	96.05	100.00	73.91			
95% CI	1.10	0.00	5.45			
Overall acc.	92.07%					
Overall 95% CI	1.24					
Kappa	0.85					

accuracy in these cases. Pan-sharpening of the SWIR1 band to derive water extents at 10 meter spatial resolution similar to Du et al. (2016) might be another possibility if Sentinel-1 data is not available. Water bodies that are covered by floating vegetation represented another issue. These cannot be detected using optical imagery alone, since the vegetation layer strongly alters the spectral profile of the underlying water. Incorporating Sentinel-1 or radar imagery with longer wavelength such as L-band or additional ancillary data might alleviate this issue (Costa et al., 2002), but requires further investigation.

Wetness was mapped less accurately than water which is due to different reasons. First, wetlands in general have less pronounced boundaries than water bodies, since there is usually a transition zone between a wetland and its drier surroundings instead of a clear boundary as it is the case for water bodies. Therefore, most omission errors occur along the edges of wetlands. An unambiguous assignment of class labels for validation points within these areas is therefore not always possible leading to the majority of omission and commission errors in the validation results. Still, user's and producer's accuracies reach values of above 75% in most cases.

One general issue when mapping wetland areas is that no unique, scientific definition of wetlands does exist (cf. Tiner, 2016). Thus, while some definitions include agricultural areas as wetlands, others do not. With the underlying approach we present a methodology to consistently detect the occurrence of open water and wet soils (wetness) serving as a pre-inventory of wetlands and building the foundation for a final wetland classification according to the user definition and needs. For the *Copernicus Pan-European HRL 2015 on Water and Wetness*, this information was directly transferred into the final classification applying a set of rules (Langanke et al., 2016). However, the method is not considered to apply a detailed nomenclature as for instance the Ramsar nomenclature. This requires to incorporate additional information on land cover and use. The WWPI can serve as a starting point to identify and delineate areas prone to wetlands (pre-inventory) and then to apply a more detailed land cover nomenclature (e.g., Ramsar definition; Tiner, 2016) to these areas. Irrespective of the various existing wetland definitions and nomenclatures, tracking long-term changes of the WWPI will allow to detect changes in the occurrence of water and wet soils in a subjective manner and independent of any definitions.

Legitimate misclassifications occasionally occur within low lying forests, very densely vegetated wetlands and peatlands. Wetness among

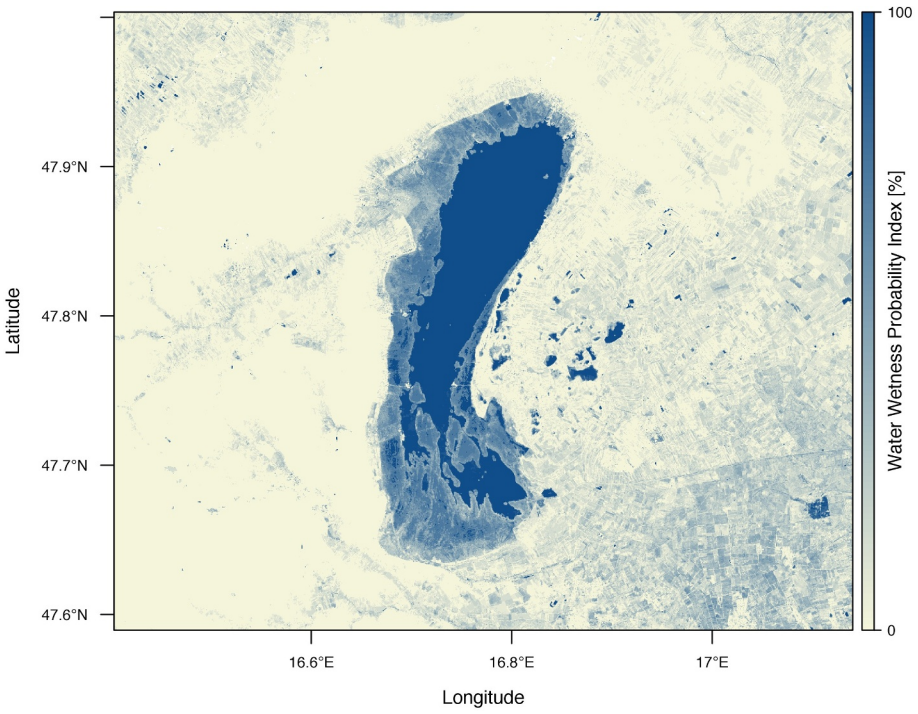

Fig. 13. Lake Neusiedl: WWPI (Jan 2016 - June 2017).

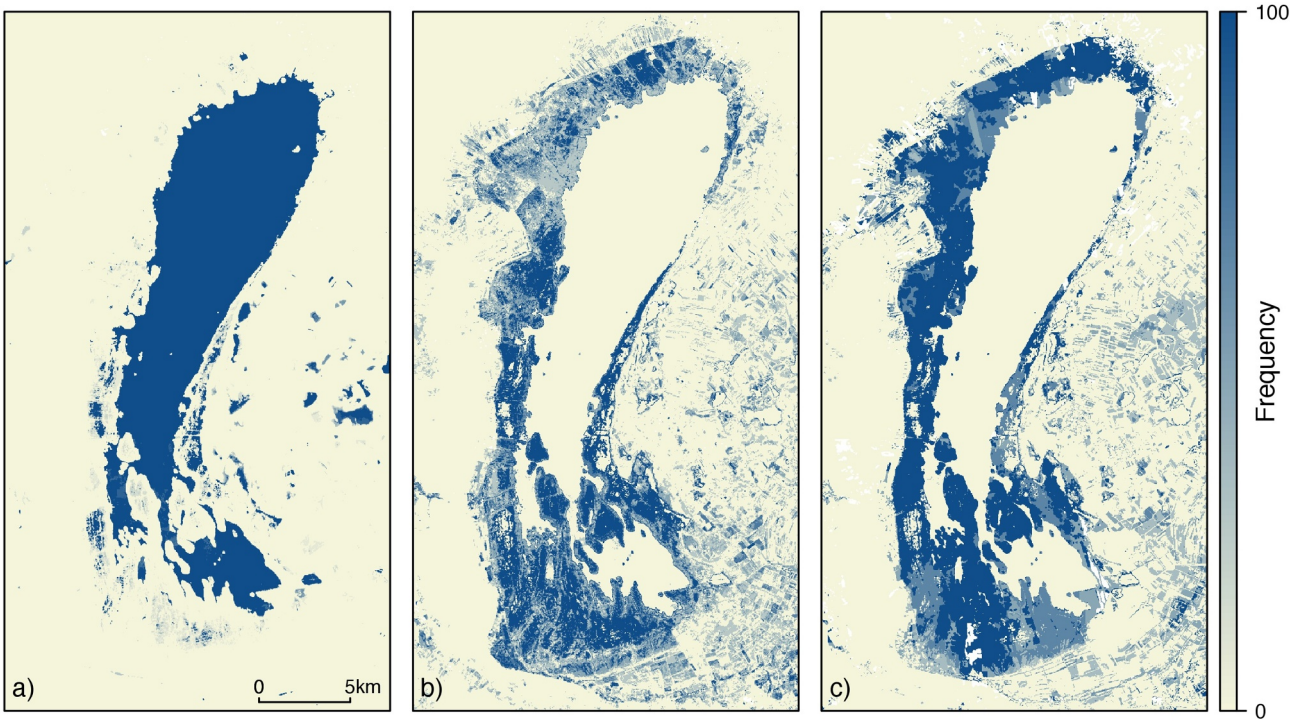

Fig. 14. Lake Neusiedl: Overall water frequency (a), and seasonal wetness frequency during summer (b) and winter (c).

peatlands is often only present at greater soil depth and only detectable right after the thawing period in spring or summer in the case of northern latitudes. As a result, contrast between the wetness of the peatland and the surrounding dry area is less pronounced reducing the capability of the algorithm to accurately delineate the wetland using optical imagery alone. In addition, the TWI cannot be applied in the case of peatlands, since their occurrence is not so much determined by topography. In this regard, further studies into the robustness and accuracy of the method for peatland mapping need to be conducted.

One possible way to increase detection rates especially for non-forested peatlands is the inclusion of soil moisture information derived from SAR imagery. First attempts in incorporating water and wetness information derived from both optical and SAR imagery, have been performed with promising results within the *Copernicus Pan-European High Resolution Layer 2015* and the ESA project *GlobWetland Africa* (Langanke et al., 2016). However, further research needs be done regarding the fusion of optical and SAR based water and wetness information that also considers the sensor-specific classification quality

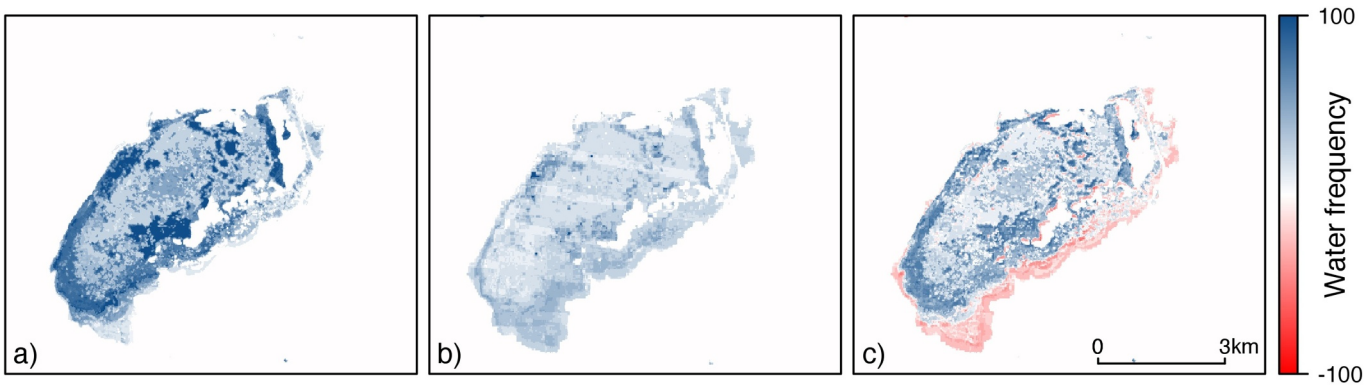

Fig. 15. The three images show Lake Tonga, a permanently flooded lake mostly covered by floating vegetation. a) Water frequency calculated in this study based on Sentinel-2 imagery from the years 2016/2017; b) seasonality of Pekel et al. (2016) based on Landsat imagery for the years 2014/2015 (converted to a water frequency scale [0,100]); c) difference in water frequency between the two classifications.

issues. Besides, it is also important to investigate the influence of the temporal resolution of the input imagery on the quality of the classification product.

Comparisons to other classification approaches that have been used for water and wetness detection show that tile-based image thresholding has considerable advantages. Classification accuracies might be slightly lower compared to supervised classification methods, however, with regard to processing time and power, the proposed method requires far less resources and is considerably faster. Another advantage compared to supervised classification methods is that this method does not require any training data for calibration. Instead, only a few parameters of the thresholding algorithm have to be evaluated and adapted in a parameter study based on a small, representative subset after which the method can be applied in a fully automated manner to a larger region. Since the algorithm can also be applied to other high resolution data such as Landsat imagery, historic analyses of long-term trends can be performed with reasonable computational and human effort.

The classification results show that the proposed method is suitable for the detection of water and wetness in different climatic regions using multi-temporal optical imagery. Water was mapped with very high accuracy (> 96%) and in a fully automatic way, since no manual adaptation of the classification parameters was required. For wet surfaces, minor adaptations of the classification parameters were necessary for each site. The validation yielded satisfying accuracy values and the final classification results convey a plausible representations of the annual water and wetness dynamics within the study sites. Considering the relation between classification quality and computational effort, the method can be seen as a first step towards the implementation of a large-scale water and wetness mapping (pre-inventory of wetlands) and monitoring service that is applicable across different bio-geographical regions.

List of abbreviations

ABDI1	Angle Based Drought Index 1
ABDI2	Angle Based Drought Index 2
ABDI	Angle Based Drought Index
ANIR	Angle at Near Infrared
AOI	Area of Interest
AWEI	Automated Water Extraction Index
AWS	Amazon Web Service
CDF	Cumulative Distribution Function
CI	Confidence Interval
DEM	Digital Elevation Model
DVW	Difference Vegetation Water
EEA	European Environmental Agency
ESA	European Space Agency
FCC	False Color Composite
Fmask	Function of mask
GDAL	Geospatial Data Abstraction Library
GLWD	Global Lakes and Wetlands Database
HAND	Height Above Nearest Drainage
HOT	Haze Optimized Transformation
HRL	High Resolution Layers
HSV	Hue-Saturation-Value
iMAD	iterative reweighted Multivariate Alteration Detection
ISODATA	Iterative Self-Organizing Data Analysis Technique
LASSO	Least Absolute Shrinkage and Selection Operator
LSWI	Land Surface Water Index
mNDWI	modified Normalized Difference Water Index
MIFW	Modified Index of Free Water
MODIS	Moderate-resolution imaging spectroradiometer
MSI	MultiSpectral Instrument
MWII	Modified Water Impoundment Index
MWI	Modified Water Index
NDBI	Normalized Difference Build-up Index
NDI	Normalized Difference Index
ND0812	Normalized Difference Index NIR-SWIR2
NDI	Normalized Difference Indices
NDMI	Normalized Difference Moisture Index
NIR	near infrared
NMDI	Normalized Multi-band Drought Index
NDVI	Normalized Difference Vegetation Index
NDWI	Normalized Difference Water Index
OLI	Operational Land Imager
RAM	Random Access Memory
RED	red spectral band
RGB	Red-Green-Blue (color model)
RMSE	Root Mean Square Error
SAGA GIS	System for Automated Geoscientific Analyses
SAR	Synthetic Aperture Radar
SASI	Shortwave Angle Slope Index
SRTM	Shuttle Radar Topography Mission
SWIR	shortwave infrared
SWIR1	shortwave infrared 1
SWIR2	shortwave infrared 2
TCBI	Tasselled Cap Brightness Index
TCGI	Tasselled Cap Greenness Index
TCWI	Tasselled Cap Wetness Index
TM	Thematic Mapper
TOA	Top-Of-Atmosphere
TWI	Topographic Wetness Index
WWF	World Wildlife Fund
WWPI	Water Wetness Presence (or Probability) Index

Acknowledgments

We would like to thank ESA for providing the funding for the GlobWetland Africa project and our colleagues at GeoVille Information Systems and Data Processing GmbH for the great support, specifically Dr. Andrew Moran, project manager for the Copernicus implementation of the Water-Wetness layer, and former staff member Steve Kass for early research activities. In addition, we are grateful to the reviewers and editors of the special issue for their valuable comments which helped to improve the quality of the original submission.

References

Beiwl, C., Mühlmann, H., 2008. Atlas der natürlichen Seen Österreichs mit einer Flächen größer gleich 50 ha: Morphometrie-Typisierung-Trophie (In German).. Bundesamt für Wasserwirtschaft.
Bennett, B., 2001. What is a forest? On the vagueness of certain geographic concepts. Topoi 20 (2), 189–201.
Beven, K.J., Kirkby, M.J., 1979. A physically based, variable contributing area model of basin hydrology. Hydrol. Sci. Bull. 24, 43–69.
Breiman, L., 2001. Random forests. Mach. Learn. 45 (1), 5–32.
Buchanan, B.P., Fleming, M., Schneider, R.L., Richards, B.K., Archibald, J., Qiu, Z., Walter, M.T., 2014. Evaluating topographic wetness indices across central New York agricultural landscapes. Hydrol. Earth Syst. Sci. 18, 3279–3299.
Bwangoy, J.-R.B., Hansen, M.C., Roy, D.P., De Grandi, G., Justice, C.O., 2010. Wetland mapping in the Congo basin using optical and radar remotely sensed data and derived topographical indices. Remote Sens. Environ. 114, 73–86.
Charman, D.J., 2002. Peatlands and Environmental Change. Wiley & Sons, London & New York.
Chen, L., Jin, Z., Michishita, R., Cai, J., Yue, T., Chen, B., Xu, B., 2014. Dynamic monitoring of wetland cover changes using time-series remote sensing imagery. Ecol. Inform. 24, 17–26.
Chen, Y., Huang, C., Ticehurst, C., Thew, P., 2013. An evaluation of MODIS daily and 8-day composite products for floodplain and wetland inundation mapping. Wetlands 24, 17–26.
Congalton, R.G., Green, K., 2008. Assessing the Accuracy of Remotely Sensed Data: Principles and Practices. CRC Press.
Corcoran, J., Knight, J., Brisco, B., Kaya, S., Cull, A., Murnaghan, K., 2011. The integration of optical, topographic, and radar data for wetland mapping in northern Minnesota. Can. J. Remote. Sens. 37 (5), 564–582.
Costa, M., Niemann, O., Novo, E., Ahern, F., 2002. Biophysical properties and mapping of aquatic vegetation during the hydrological cycle of the Amazon foodplain using JERS-1 and Radarsat. Remote Sens. 23 (7), 1401–1426.
Das, P.K., Sahay, B., Seshasai, M.V.R., Dutta, D., 2017. Generation of improved surface moisture information using angle-based drought index derived from Resourcesat-2 AWiFS for Haryana state, India. Geomat. Nat. Haz. Risk 8, 271–281.
Davranche, A., Poulin, B., Lefebvre, G., 2013. Mapping flooding regimes in Camargue wetlands using seasonal multispectral data. Remote Sens. Environ. 138, 165–171.
Dogan, O.K., Akyurek, Z., Beklioglu, M., 2009. Identification and mapping of submerged plants in a shallow lake using Quickbird satellite data. J. Environ. Manag. 90 (7), 2138–2143.
Donchyts, G., Schellekens, J., Winsemius, H., Eisemann, E., van de Giesen, N., 2016. A 30 m resolution surface water mask including estimation of positional and thematic differences using Landsat 8, SRTM and OpenStreetMap: a case study in the Murray-Darling Basin, Australia. Remote 8.
Du, Y., Zhang, Y., Ling, F., Wang, Q., Li, W., Li, X., 2016. Water bodies' mapping from sentinel-2 imagery with modified normalized difference water index at 10-m spatial resolution produced by sharpening the SWIR band. Remote Sens. 8 (4), 354–373.
Erwin, K.L., 2009. Wetlands and global climate change: the role of wetland restoration in a changing world. Wetl. Ecol. Manag. 17 (1), 71.
European Space Agency, 2015. Sentinel-2 User Handbook.
Farr, T.G., Rosen, P.A., Caro, E., Crippen, R., Duren, R., Hensley, S., Kobrick, M., Paller, M., Rodriguez, E., Roth, L., et al., 2007. The shuttle radar topography mission. Rev. Geophys. 54 (2).
Feyisa, G.L., 2014, January, January. Automated water extraction index: a new technique for surface water mapping using Landsat imagery. Remote Sens. Environ. 140, 23–35.
Fluet-Chouinard, E., Lehner, B., Rebelo, L.-M., Papa, F., Hamilton, S.K., 2015. Development of a global inundation map at high spatial resolution from topographic downscaling of coarse-scale remote sensing data. Remote Sens. Environ. 158, 348–361.
Gao, B.-C., 1996. NDWI - a normalized difference water index for remote sensing of vegetation liquid water from space. Remote Sens. Environ. 58, 257–266.
Guo, B., Damper, R.I., Gunn, S.R., Nelson, J.D.B., 2008. A fast separability-based feature selection method for high-dimensional remotely-sensed image classification. Pattern Recogn. 41 (5), 1653–1662.
Gutman, G.G., Ignatov, A.M., Olson, S., 1994. Towards better quality of AVHRR composite images over land: reduction of cloud contamination. Remote Sens. Environ. 50 (2), 134–148.
Holben, B.N., 1986. Characteristics of maximum value composite images for temporal AVHRR data. Int. J. Remote Sens. 7, 1417–1437.
Islam, M.A., Thenkabail, P.S., Kulawardhana, R., Alankara, R., Gunasinghe, S., Edussriya, C., Gunawardana, A., 2008. Semi-automated methods for mapping wetlands using Landsat ETM+ and SRTM data. Int. J. Remote Sens. 29 (24), 7077–7106.
Jiang, H., Feng, M., Zhu, Y., Lu, N., Huang, J., Xiao, T., 2014. An automated method for extracting rivers and lakes from Landsat imagery. Remote Sens. 6, 5067–5089.
Jiang, Z., Qi, J., Su, S., Zhang, Z., Wu, J., 2011. Water body delineation using index composition and his transformation. Remote Sens. 33 (11), 3402–3421.
Junk, W.J., An, S., Finlayson, C.M., Gopal, B., Květ, J., Mitchell, S.A., Mitsch, W.J., Robarts, R.D., 2013. Current state of knowledge regarding the world's wetlands and their future under global climate change: a synthesis. Aquat. Sci. 75 (1), 151–167.
Khannaa, S., Palacios-Oruetaa, A., Whitinga, M.L., Ustina, S.L., Riañoa, D., Litago, J., 2007. Development of angle indexes for soil moisture estimation, dry matter detection and land-cover discrimination. Remote Sens. Environ. 109, 154–165.
Kottek, M., Grieser, J., Beck, C., Rudolf, B., Rubel, F., 2006. 2006: World map of the Köppen-Geiger climate classification updated. Meteorol. Z. 259–263.
Kulawardhana, R.W., Thenkabail, P.S., Vithanage, J., Biradar, C., Islam, Md.A., Gunasinghe, S., Alankara, R., 2007. Evaluation of the wetland mapping methods using Landsat ETM+ and SRTM data. J. Spat. Hydrol. 7 (2), 62–96.
Landmann, T., Schramm, M., Colditz, R.R., Dietz, A., Dech, S., 2010. Wide area wetland mapping in semi-arid Africa using 250-meter modis metrics and topographic variables. Remote Sens. 2, 1751–1766.
Lane, C.R., Liu, H., Autrey, B.C., Anenkhonov, O.A., Chepinoga, V.V., Wu, Q., 2014. Improved wetland classification using eight-band high resolution satellite imagery and a hybrid approach. Remote Sens. 6 (12), 12187–12216.
Langanke, T., Moran, A., Dulleck, B., Schleicher, C., 2016. Copernicus land monitoring service — high resolution layer water and wetness: product specifications document. In: Technical Report. European Environment Agency.
Li, J., Chen, W., 2005. A rule-based method for mapping Canada's wetlands using optical, radar and DEM data. Remote Sens. 26 (22), 5051–5069.
Li, W., Du, Z., Ling, F., Zhou, D., Wang, H., Gui, Y., Sun, B., Zhang, X., 2013. A comparison of land surface water mapping using the normalized difference water index from TM, ETM+ and ALI. Remote Sens. 5, 5530–5549.
Louis, J., Debaecker, V., Pflug, B., Main-Knorn, M., Bieniarz, J., Mueller-Wilm, U., Cadau, E., Gascon, F., 2016. Sentinel-2 sen2cor: L2a processor for users. In: Ouwehand, L. (Ed.), ESA Living Planet Symposium 2016. ESA Special Publications (on CD), vol. SP-740. Spacebooks Online, pp. 1–8.
Luo, Y., Trishchenko, A., Khlopenkov, V., 2008. Developing clear-sky, cloud and cloud shadow mask for producing clear-sky composites at 250-meter spatial resolution for the seven MODIS land bands over Canada and North America. Remote Sens. Environ. 112, 4167–4185.
Lück, W., Van Niekerk, A., 2016. Evaluation of a rule-based compositing technique for Landsat-5 TM and Landsat-7 ETM+ images. Int. J. Appl. Earth Obs. Geoinf. 47, 1–14.
Martinis, S., Twele, A., Voigt, S., 2009. Towards operational near-real time flood detection using a split-based automatic thresholding procedure on high resolution TerraSAR-X data. Nat. Hazards Earth Syst. Sci. 9, 303–314.
McFeeters, S.K., 1996. The use of the Normalized Difference Water Index (NDWI) in the delineation of open water features. Int. J. Remote Sens. 17 (7), 1425–1432.
MEMR, 2012. Kenay Wetlands Atlas. MEMR Ministry of Environment and Mineral Resources, Kenya, P.O. Box 30126-00100, Nairobi, Kenya.
Mwita, E., Menz, G., Misana, S., Nienkemper, P., 2012. Detection of small wetlands with multi sensor data in east Africa. Adv. Remote Sens. 1, 64–73.
Olofsson, P., Foody, G.M., Herold, M., Stehman, S.V., Woodcock, C.E., Wulder, M.A., 2014. Good practices for estimating area and assessing accuracy of land change. Remote Sens. Environ. 148, 42–57.
Orodyne, C., Friedl, M.A., 2008. Using MODIS data to characterize seasonal inundation patterns in the Florida Everglades. Remote Sens. Environ. 112, 4107–4119.
Otsu, N., 1975. A threshold selection method from gray-level histograms. Automatica 11 (285–296), 23–27.
Ozesmi, S.L., Bauer, M.E., 2002. Satellite remote sensing of wetlands. Wetl. Ecol. Manag. 10, 381–402.
Pekel, J.-F., 2014. A near real-time water surface detection method based on HSV transformation of MODIS multi-spectral time series data. Remote Sens. Environ. 540, 418–422.
Pekel, J.-F., Cottam, A., Gorelick, N., Belward, A.S., 2016. High-resolution mapping of global surface water and its long-term changes. Nature 540, 418–422.
Ramsar Convention, 2001. Ramsar Sites Information Service. , Accessed date: 18 December 2016.
Ramsar Convention, 2016. An Introduction to the Ramsar Convention on Wetlands, 7th ed. Ramsar Convention Secretariat, Gland, Switzerland.
Rokni, K., Ahmad, A., Selamat, A., Hazini, S., 2014. Water feature extraction and change detection using multitemporal Landsat imagery. Remote Sens. 6, 4173–4189.
Rouse, J., Haas, R., Scheel, J., Deering, D., 1974. Monitoring vegetation systems in the great plains with ERTS. In: Proceedings, 3rd Earth Resource Technology Satellite (ERTS) Symposium. Proceedings, 3rd Earth Resource Technology Satellite (ERTS) Symposium, vol. 1. pp. 48–62.
Smart, M., Hollis, G., 1990. Ramsar advisory missions: report no. 21, Algeria. In: Technical Report 21. Ramsar Convention of Wetlands.
Tana, G., Letu, H., Cheng, Z., Tateishi, R., 2013. Wetlands mapping in North America by decision rule classification using modis and ancillary data. IEEE J. Sel. Top. Appl. Earth Obs. Remote Sens. 6 (6), 2391–2401.

Tetteh, G.O., Schönert, M., 2015. Automatic generation of water masks from RapidEye images. J. Geosci. Environ. Protect. 3, 17–23.
Tiner, R.W., 2016. Wetland Indicators: A Guide to Wetland Formation, Identification, Delineation, Classification, and Mapping. CRC Press.
Tiner, R.W., Lang, M.W., Klemas, V.V. (Eds.), 2015. Remote Sensing of Wetlands: Applications and Advances. Taylor and Francis Group.
Wang, L., Qu, J.J., 2007. NMDI: a normalized multi-band drought index for monitoring soil and vegetation moisture with satellite remote sensing. Geophys. Res. Lett. 34 (20).
World Wildlife Fund, 2016. Global Lakes and Wetlands Database. , Accessed date: 29 December 2016.
Xu, H., 2006, July, July. Modification of normalized difference water index (NDWI) to enhance open water feature in remotely sensed imagery. Int. J. Remote Sens. 27 (14), 3025–3033.
Zhao, B., Yan, Y., Guo, H., He, M., Gu, Y., Li, B., 2009. Monitoring rapid vegetation succession in estuarine wetland using time series MODIS-based indicators: an application in the Yangtze River Delta area. Ecol. Indic. 9, 346–356.
Zhu, Z., Woodcock, C.E., 2014. Automated cloud, cloud shadow, and snow detection in multitemporal Landsat data: an algorithm designed specifically for monitoring land cover change. Remote Sens. Environ. 152, 217–234.